Model Calculation for Radiation Damage of Diamond Detector

M. Mishina

Fermilab

May 21, 1999

A simple model was developed to simulate the decrease of diamond detector response observed after exposure to large dose of radiation. The model assumes that the irradiation creates charge traps uniformly over the diamond material in addition to the preexisted charge traps inherent to CVD diamond. These additional charge traps were incorporated into a version of so-called "linear model[1)] " formulated in the previous work[2)] which assumes a charge absorption length that grows linearly with the growth of diamond thickness from substrate surface. Such model was found to reproduce the reported general behavior of diamond samples with respect to the exposed dose for pion and neutron irradiation. In the case of neutron irradiation, the observed relative shrinkage of the pulse height distribution due to the irradiation was studied further incorporating Landau fluctuation of the energy deposit. Once the input parameters of the calculation is adjusted to reproduce the shape of the observed pulse height distribution much wider than what is expected from Landau distribution before the irradiation, the pulse height distribution after the irradiation was well reproduced by only changing the radiation induced charge absorption length from zero to the value found by the fit to the corresponding collection distance.

1. INTRODUCTION

Since the major advantage of using CVD diamond as vertex detector is its radiation hardness predictable from the large bandgap, there have been series of irradiation studies of CVD diamond by protons[3)], pions (Vienna group[4)]) and neutrons (R. Wedenig *et. al.*[5)]). The energy or momentum of these incident particles were chosen to be at the energy of the dominant background in hadron collider environment, i. e., 10 GeV for protons, 300 MeV/c for π^+'s, and 1 MeV in kinetic energy for neutrons. With significant amount of data already accumulated in wide range of fluence up to ~10^{15} particles/cm^2, it is highly desirable to have some understanding of how the radiation damages diamond at least phenomenologically and to try to find systematic formula that describe the decrease of the response with increasing fluence.

Among the data for these incident particles, we found the behavior of proton irradiation data somewhat peculiar even showing initial increase of the response in low dose followed by a plateau and decrease at very high dose indicating complication not necessarily a direct result of radiation damage. Therefore we concentrate to the π^+ and the neutron irradiation data which show similar pattern.

The pattern common to the π^+ and the neutron irradiation data at and above a few x 10^{14} particles/cm^2 are:

- Samples of greater signals, either due to greater thickness or better material quality, showed a faster decrease of the signal with increasing radiation dose than for the samples of smaller signals.
- For a given sample, the pulse height distribution appeared to shrink faster in the higher

pulse height portion of the spectrum making the shape of the pulse height spectrum *narrower* in relative scale.

Since the studied range of the radiation dose is already well in the level required for the assumed 10-year operation of the LHC at full luminosity, combination of the above observations A) and B), implicate that the detection efficiency which is sensitive to the lower side of the most probable peak of the spectrum is not as significantly affected by the radiation as it appears, and conversely we may be able to make a target for the optimum combinations of material parameters.

In this report, we study the following issues:

- Can the observed behavior be reproduced by a model derived from the "first principles" with minimum number of adjustable input parameters ?
- Is the general behavior of the radiation damage universal independent of the material ?
- Are there any combinations of the parameters such as the coefficient of the "linear term",*c* , thickness, the thickness lapped off from substrate side, etc., optimum to provide best durability against radiation damage ?
- If the general behavior can be understood, it is desirable to deduce the dependence of the detection efficiency as a function of the radiation dose or conversely to deduce desirable material quality that guarantees high enough detection efficiency.

The "first principles" we rely on are:

1) We assume the "Linear Model" as the charge absorption inherent to CVD diamond. The model, as described in detail in the previous paper[2], assumes that the local charge absorption length grow linearly with the depth measured from the original substrate side. (For general discussion, readers are referred to Ref. 2))
2) We assume that the "charge traps" created as a result of radiation damage
   a) have a uniform density over the depth.
   b) with the density proportional to the dose.

   Therefore it can be parametrized by a single charge absorption length, constant over the depth, which is inversely proportional to the dose.

   Note : i) It is implicitly assumed here that the density of carbon atoms is uniform over the volume in question.
   ii) The effect of the radiation on the pre-existing charge traps is assumed to be negligible compared to the effect by newly created charge traps[6] .

As studied in the previous work, we have some evidence that the linear model is a reasonably correct description of the charge transmission properties of CVD diamond.The radiation damage ought to be the result of nuclear interactions and therefore it is natural to take the above assumption 2 b).

2. MODEL FORMULATION

The local charge absorption due to uniformly distributed charge traps can be parametrized by a constant charge absorption length λ_{rad} in the following exponential form:

$$\exp\left(-\frac{|z'-z|}{\lambda_{rad}}\right) \qquad (1)$$

where z' : point of charge creation,
z : position of the drifting charge.

As derived in Appendix 1, this ought to be a multiplicative factor over the "linear" charge absorption factor inherent to CVD diamond layer:

$$\left(\frac{\zeta}{\zeta'}\right)^{\frac{1}{c}} \qquad (2).$$

Where ζ' : point of charge creation measured from the original substrate side surface.

ζ : position of drifting charge measured from the original substrate side surface.

Here the local charge absorption length $\lambda_{CVD}(\zeta)$ is assumed to grow linearly with the depth ζ measured from the original substrate side surface as

$$\lambda_{CVD}(\zeta) = c\zeta \qquad (3)$$

where c : constant,

based on "linear model". Using the as-grown thickness T, ζ and ζ' can be replaced by T-z and T-z', respectively.

The net charge absorption factor is therefore as follows:

$$\left(\frac{T-z}{T-z'}\right)^{\frac{1}{c}} \exp\left(-\frac{z-z'}{\lambda_{rad}}\right) \quad \text{or} \quad \left(\frac{T-z'}{T-z}\right)^{\frac{1}{c}} \exp\left(-\frac{z'-z}{\lambda_{rad}}\right) \qquad (4)$$

depending on whether the deposited charge is moving away from the growth side or towards the growth side. (See Appendix for step by step deduction of the above formula.) We take a convention in which the origin of z-coordinate is on the surface of the growth side.

Since it is trivial to show that the magnitude of the *total* induced charge is independent of the direction of the motion, or in other words the polarity of the electric field, the rest of the discussion is for the case of the charge moving away from the electrode.

The charge induced by the local motion of the drifting charge is a product of the charge and the drift distance normalized by D, the gap of the two electrodes on the surface after possible lapping on the substrate side.

The charge at position z initially deposited at position z' is the product of the initially deposited charge $\frac{dQ_{deposited}}{dz'}$ and the attenuation from z' to z as given by eq. (4). The resulting total induced charge can be calculated by carrying out the double integration over z' and z, which takes into account both the position of the charge deposition and its attenuation as a function of drift distance. Therefore the total induced charge can be written as follows:

$$Q_{induced}^{total} = \frac{1}{D}\int_{z'=0}^{D} dz' \int_{z=z'}^{D} dz \frac{dQ_{deposited}}{dz'} \left(\frac{T-z}{T-z'}\right)^{\frac{1}{c}} \exp\left(-\frac{z-z'}{\lambda_{rad}}\right).$$

Assuming that the density , and therefore the energy deposit, is uniform,

$$= \frac{1}{D}\frac{dQ_{deposit}}{dz'} \int_{z'=0}^{D} dz' \int_{z=z'}^{D} dz' \left(\frac{T-z}{T-z'}\right)^{\frac{1}{c}} \exp\left(-\frac{z-z'}{\lambda}\right). \qquad (5)$$

It should be noted that for the charge drifting towards the growth side, eq. (5) is rewritten as follows:

$$Q_{induced}^{total} = \frac{1}{D}\frac{dQ_{deposit}}{dz'} \int_{z'=0}^{D} dz' \int_{z=z'}^{0} dz \left(\frac{T-z'}{T-z}\right)^{\frac{1}{c}} \exp\left(-\frac{z'-z}{\lambda_{rad}}\right). \qquad (6)$$

The result of the integration is exactly the same, except for the sign, as the case of charge drifting away from the growth side.

There is an issue of the nature of charge traps created by irradiation. In principle, the charge traps due to radiation damage can react differently to electrons and holes and thus causing different charge absorption lengths. However introducing two independent charge absorption lengths would simply obscure the conclusion with the limited number of the data points and the accuracy. Therefore we assume a single *effective* charge absorption length common to electrons and holes.

It should also be pointed out that the charge collection distance is dependent on the applied field and whether the sample is "pumped". However, since the correct description of the condition to reach the saturated plateau is not known, it is a useless complication to take such conditions other than the saturated points into account. The pion and neutron irradiation data are taken properly at the saturated point thus allowing us to deal with the data in a well defined condition.

3. CALCULATED RESULTS

3.1 General trend

In order to study the general trend, we take an example of the final thickness *D* of 300 μm and as-grown thickness *T* of 1 mm and 2 mm. The value of c was taken as 0.1. 0.2, and 0.3 and the radiation induced charge absorption length was varied in the range of 10 μm and 10^6 μm. The integration was carried out numerically. The result is plotted in Fig. 1. The horizontal axis is $1/\lambda_{rad}$, which is assumed to be directly proportional to the radiation dose.

In this graph it is seen that significant change in the induced signal occurs in the range of 100 μm to 1000 μm in the radiation induced absorption length. This is naturally expected because the effect is a competing process against the pre-existing linear absorption length which is in the similar range. Also obvious is that the curves for greater signals, irrespective of whether due to greater thickness or due to greater values of *c*, tend to decrease rapidly with increasing radiation dose while the relative decrease of the curves for smaller signals is less significant. The fact that there is no crossing among the curves indicates that there is no optimum choice in the parameter set of the thickness, how it is lapped, and the value of *c* to make the diamond detector more resistant against damage while maintaining necessary signal size. Curves that start with greater values of the signals always maintain to be greater in the magnitude of the signal but the relative advantage diminishes at higher dose.

The results shown in Fig. 1 are re-plotted in Fig. 2 with linear scale of radiation dose. One can see that in this model the decrease of the signal is a continuous process as intuitively expected and there is no "threshold" in radiation dose from which the signal starts decreasing. The figure also shows that the relative decrease in signal size is rapid initially.

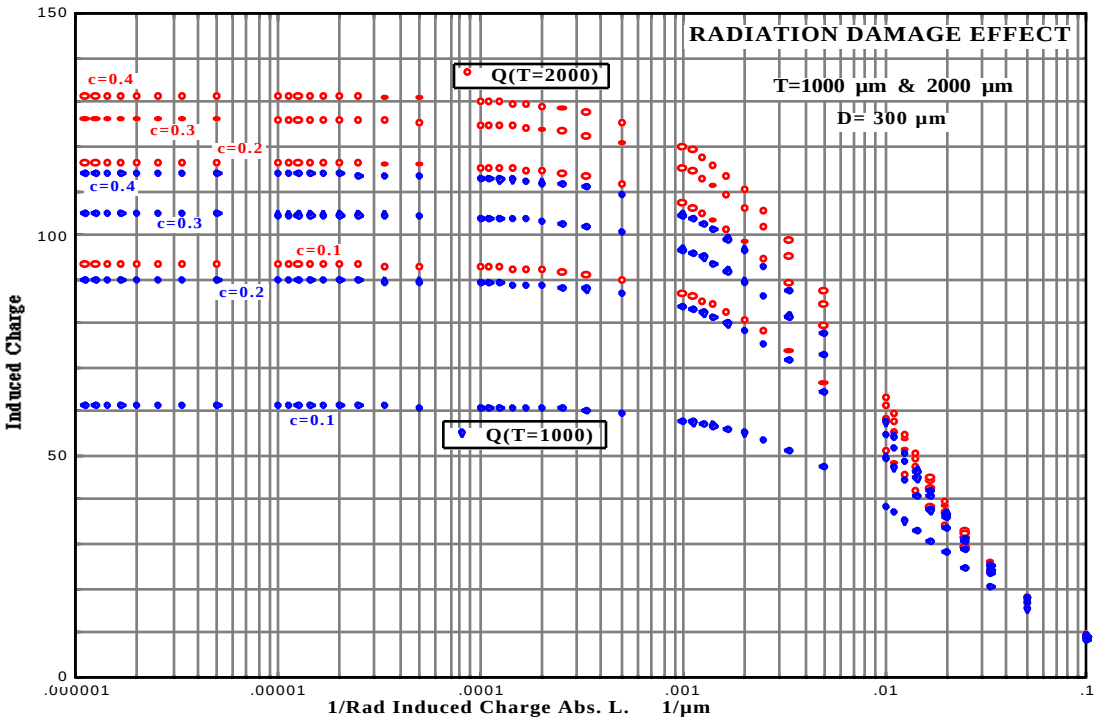

Fig. 1. Plot of the induced charge against $1/\lambda_{rad\ \text{which}}$, which is assumed to be directly proportional to the radiation dose.

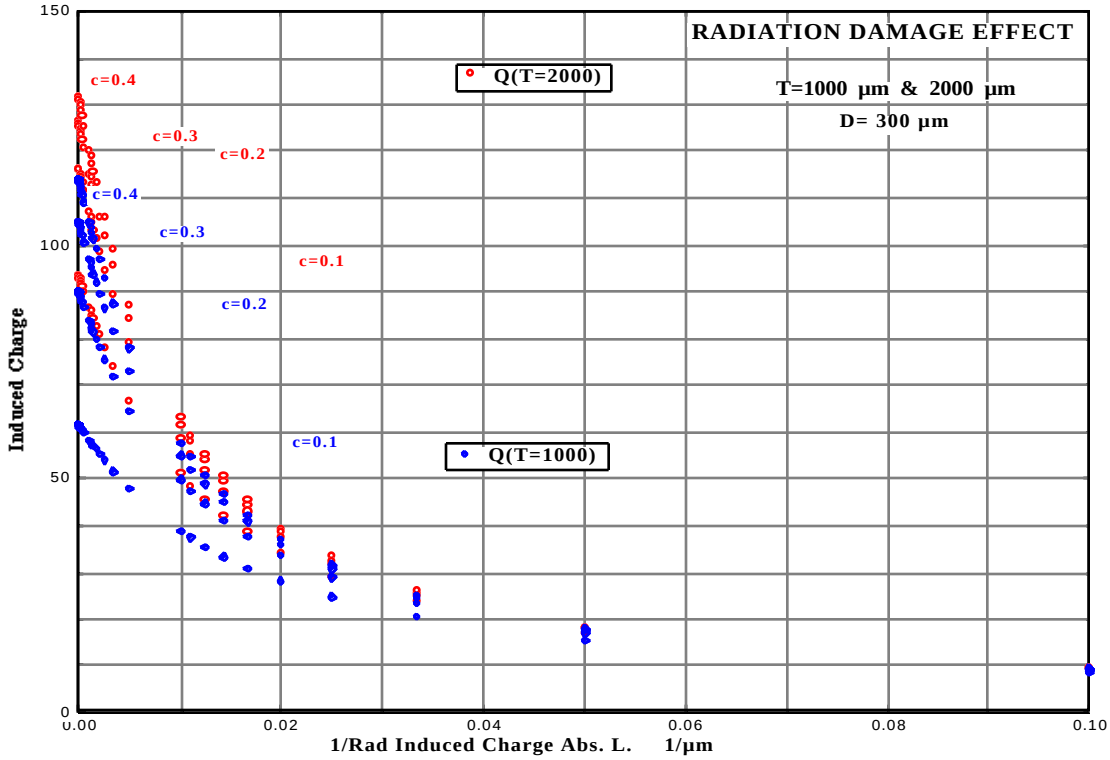

Fig. 2. The same graph as the above re-plotted with a linear scale in the horizonal axis.

3.2 General strategy for examining experimental data

When we examine experimental data of pion and neutron irradiation in the following, we float a single parameter as the factor to convert fluence into to charge absorption length for each of the data sets of pion and neutron irradiation and seek for the best fit for all of the data points within the set. In case of pion irradiation data, the linear coefficient *c* of each of the samples was fixed to the value derived from zero-fluence data point. For neutron irradiation case, the value of *c* of each of the sample was floated to have the best fit to all the data points of the sample for the given conversion factor.

3.3 Pion irradiation data

Next we calculate the curves corresponding to the data of pion irradiated samples. The parameters of the samples, listed in Table 1, are based on the data presented by M. Friedle in the past meetings for the Vienna group with additional information on the thickness of the samples provided by M. Friedle.

Table 1: Pion irradiated CVD diamond samples.

The data on the radiation dose and the collection distance in this table is from Table 3 of RD42 Note by the Vienna group. The thickness of the samples before and after lapping is provided by M. Friedle. The values of the coefficient *c* in parentheses are calculated based on the thickness and the collection distance thus given. Equal contributions from electrons and holes are assumed.

Sample	Thickness		Total Fluence	Collection Distance μm (c)				
	As-grown	Final	10^{15} π/cm^2	Vienna		CERN		OSU
TD1038-U3	447	447	0	-		-		47 (0.1176)
			1.811	31		49		-
TD1038-U4	430	430	0	-		-		47 (0.1228)
			0.675	47		-		-
DBDS 43-P1	737	737	0	85	(0.1304)	103	(0.1625)	78 (0.1184)
			1.423	62		60		-
DBDS 43-P2	760	760	0	-		90	(0.1344)	94 (0.1412)
			1.898	57		61		-
DBDS 73-R1	1098	603	0	176	(0.1366)	167	(0.1278)	-
			1.033	101		104		-
DBDS 73-R2	1098	611	0	173	(0.1339)	183	(0.1438)	-
			1.055	103		-		-
DBDS 74-P1	1055	611	0	119	(0.0905)	133	(0.1030)	-
			1.096	92		95		-
DBDS 74-P2	1055	641	0	160	(0.1302)	183	(0.1539)	-
			1.035	104		118		-
DBDS 83	780	690	0	140	(0.1933)	197	(0.2971)	-
-Tracker			1.045	74		122		-

We use Vienna data as much as possible in order to be consistent with the presented graph for the calculation of the coefficient *c* and also for fitting. If Vienna group's data is not listed, we use CERN data and OSU data, in respective order.

Given the parameters, what is not known is the conversion between the fluence and the absorption length λ_{rad}. Therefore we search for the best fit to the nine data points of collection distance vs. fluence, after the irradiation to determine the conversion factor. The nine initial points before the irradiation and the coefficient *c* for each of the samples derived

from those points are fixed. The only adjustable parameter is the conversion factor, which is defined as

$$\text{conversion factor} = \frac{\left(\frac{1}{\lambda_{rad}(\mu m)}\right)}{Fluence(10^{15}\ particles/cm^2)} . \qquad (7)$$

Since we do not have the values for the errors assigned to the data, we simply use a least square fit.

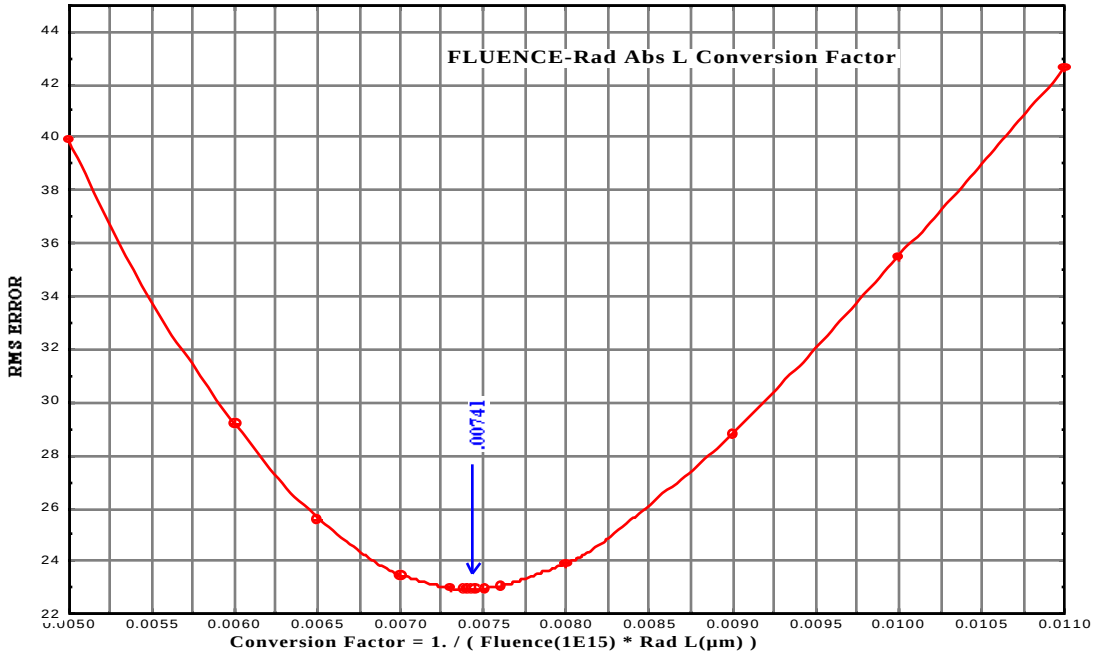

Fig. 3. Variance of nine data points against the fluence to absorption length conversion factor.

The total variance of the nine data points is plotted in Fig. 3 as a function of the conversion factor. From this we find 0.00741 as the most plausible value of the conversion factor.

Using this value, the calculated collection distance as a function of the fluence for each of the nine samples is plotted in Fig. 4 superimposed over the data measured by the Vienna group. Since the data presented by the Vienna group included the other points with lower fluence than the total accumulated fluence listed in Table 1, we used the scanned image of the graph presented by the Vienna group. It is seen that the overall trend of the data is reasonably well reproduced by the calculation, especially when one considers the possible uncertainties, a measure of which is the point to point fluctuation. The scale on the top is the radiation induced absorption length corresponding to the fluence. It is clearly seen that the range of significant decrease in the response corresponds to the radiation induced absorption length comparable to or smaller than the pre-existed absorption length.

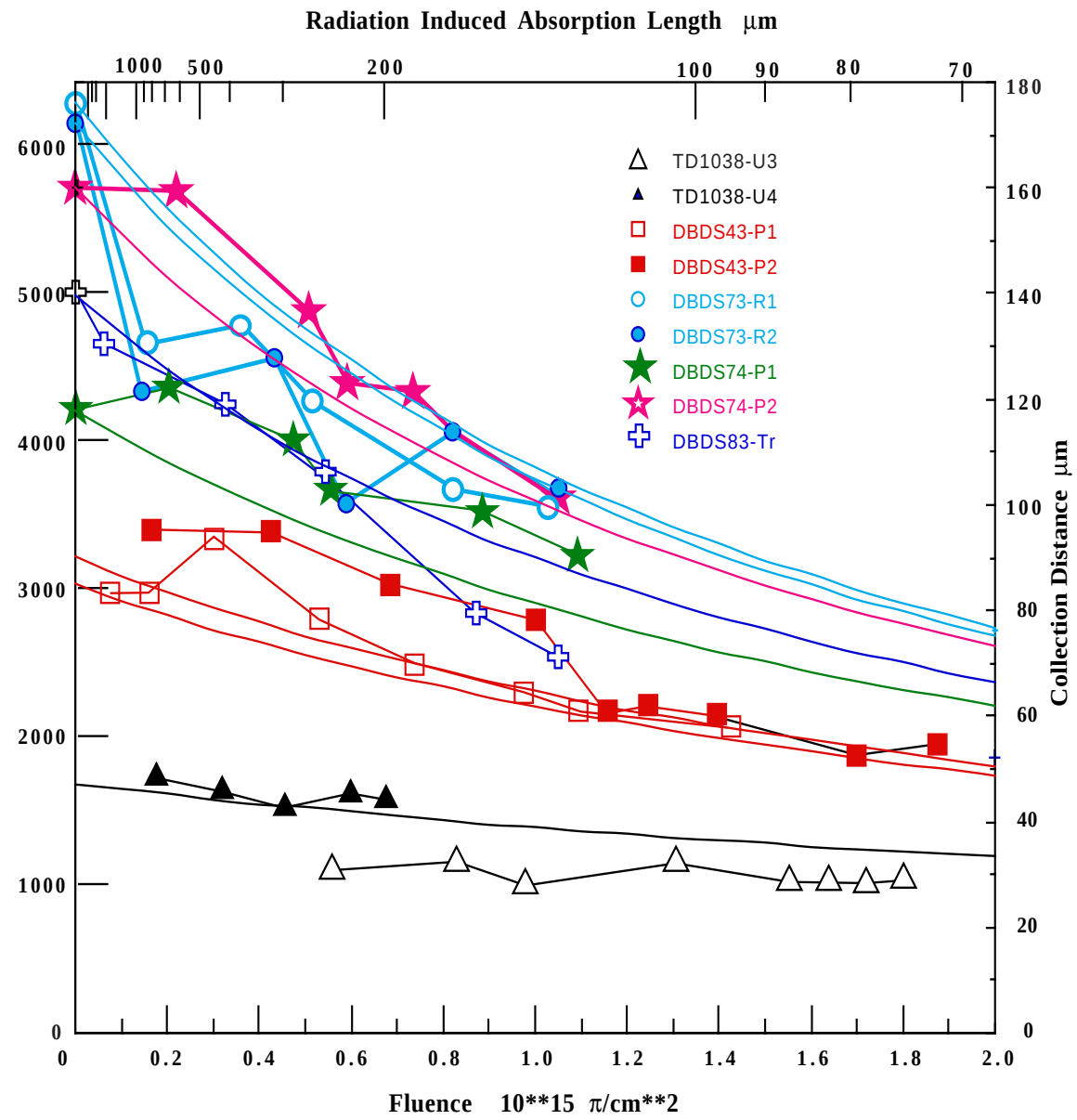

Fig. 4. Calculated curves overlaid on pion irradiation data by the Vienna group.

3.4 Neutron irradiation data

The data for the neutron irradiated samples are from the presentation by R. Wedenig with additional information on the thickness provided by R. Wedenig. Table 2 lists the parameters of those samples. The data on the radiation dose and the collection distance in this table is mainly from the presentation by R. Wedenig at RD42 meeting at CERN on April 27-28, 1998. In addition R. Wedenig provided us thickness data and other data points which are not listed in the original table but were in the graph shown in the presentation. Coefficient *c* for each sample was calculated from the given thickness and the collection distance measured at zero fluence.

Table 2. Neutron irradiated diamond samples. (* denotes that the values were read out from the original graph of Wedenig. et. al. .)

Sample	Thickness		Total Fluence	Collection Distance	(c)
	As-grown	Final	10^{15} n/cm^2 (>10keV)	μm	
DB 81-P1	1202	640	0	128.19 ± 3.05	(0.0829)
			0.293 ± 0.05	89.18 ± 5.04	
DB 81-P2	1202	640	0	163.42 ± 5.34	(0.1106)
			0.417 ± 0.06	69.41 ± 2.69	
DB 81-P3	1202	640	0	156.17 ± 5.88	(0.1047)
			0.568 ± 0.13	62.43 ± 1.33	
DB 43-P3	755	755	0*	99* ± 1*	(0.1509*)
			0.13 ± 0.02*	88.01 ± 3.44	
			0.423 ± 0.05	75.3 ± 2.02	
DB 43-p4	755	755	0*	86* ± 1.5*	(0.1286*)
			0.19 ± 0.05*	70.60 ± 2.49	
			0.758 ± 0.13	48.68 ± 1.58	
U6	435	435	0	52 ± 4	(0.1358)
			0.317 ± 0.058	51 ± 4	
			0.485 ± 0.061	50.37 ± 1.84	
			0.877 ± 0.09	30.46 ± 1.19	
U7	433	433	0	55 ± 4	(0.1455*)
			0.545 ± 0.179	48 ± 4*	
			0.75 ± 0.189	38.89 ± 1.87	
			1.318 ± 0.13	33.29 ± 0.93	
N1	329	329	0*	45* ± 4*	(0.1585*)
			0.40* ± 0.08*	46* ± 4*	
			0.51 ± 0.075	40.32 ± 2.75	
			0.51 ± 0.075	43.78 ± 1.44	
N2	333	333	0*	44* ± 4*	(0.1523*)
			0.40* ± 0.08*	45* ± 4*	
			0.57 ± 0.08*	38.33 ± 2.93	
			0.987 ± 0.06	30.97 ± 1.28	
N3	354	354	0*	36* ± 4*	(0.1132*)
			0.54* ± 0.18*	32* ± 4*	
			0.73 ± 0.19	32.2 ± 0.9	
			1.298 ± 0.13	20.08 ± 0.9	

Since uncertainties were assigned to the measured collection distances and the neutron fluence values we can use χ^2 to search the best fit. In the manner similar to the case of the pion irradiation data, we vary the fluence-to-absorption length conversion factor

for each value we calculate the χ^2 for each measured points. The definition of the conversion factor is identical to (7) with the fluence being the neutron fluence. However, this time, the value of coefficient *c* for each sample is floated to give the minimum χ^2 for each sample for the given value of conversion factor and the χ^2 's were summed to calculate the total χ^2.

Four methods were tried in the χ^2-minimum fitting.

Method A) : The uncertainty in the fluence was taken into account for the total uncertainty of each data point in the following manner:

$$\sigma^2_{total} = \sigma^2_{D_c} + \left(\frac{1}{2}\left\{ D_c\left(fluence - \sigma_{fluence}\right) - D_c\left(fluence + \sigma_{fluence}\right)\right\}\right)^2 \quad (8)$$

where

$D_c(fluence \pm \sigma_{fluence})$

is the collection distance calculated for the fluence of

$fluence \pm \sigma_{fluence}$. .

and the total χ^2 was the sum of χ^2 's of the collection distance using the σ_{tota}

defined above.

Method B) : This was to minimize the shortest distance from the data point to the calculated curve. In χ^2 calculation for each data point, the collection distance was calculated at the nominal fluence of the corresponding data point.

$$\chi^2_D(sample_i, data_j) = \left(\frac{D_{calc}(sample_i, data_j) - D_{meas}(sample_i, data_j)}{\sigma_D(sample_i, data_j)}\right)^2$$

where D_{calc} ($sample_i$, $datai_j$) is the collection distance calculated for the $sample_i$ for the nominal fluence of the$data_j$.

For the χ^2 of the fluence, the calculated fluence was the fluence of the point, on the calculated curve, that gives the nominal collection distance of the data.

$$\chi^2_{fluence}(sample_i, data_j) = \left(\frac{fluence_{calc}(sample_i, data_j) - fluence_{meas}(sample_i, data_j)}{\sigma_{fluence}(sample_i, data_j)}\right)^2$$

where $fluence_{calc}(sample_i, data_j)$ is the fluence at which $D_{calc}(fluence_{calc}(sample_i, data_j)) = D_{meas}(sample_{i,} data_j)$.

For the points of zero fluence, only the χ^2 of the collection distance was used.

Method C) : Same as the above except that for the zero fluence points, the χ^2 of the collection distance was counted twice.

Method D) : As an extreme case, only the two samples with highest collection distance at zero fluence, i. e., DBDS 81- P2 and DBDS 81-P3, were fitted. Only the χ^2 of the collection distance was evaluated.

The results returned by the fitting program are listed in Table 3.

As expected, Method D) returned the values of *c* close to the values calculated from the zero fluence points as listed in Table 2.

Table 3. Values returned by χ^2 -minimum fitting.

		Method A)	Method B)	Method C)	Method D)
Conversion Factor (μm•10^{15} n/cm^2)$^{-1}$		0.0221	0.0253	0.0252	0.0380
c	DBDS 81-P1	0.0828	0.0831	0.0830	
	DBDS 81-P2	0.1077	0.0928	0.0989	0.1111
	DBDS 81-P3	0.1038	0.0841	0.0900	0.1050
	DBDS 43-P3	0.1521	0.1541	0.1524	
	DBDS 43-P4	0.1287	0.1307	0.1298	
	U 6	0.1514	0.1608	0.1589	
	U 7	0.1649	0.1921	0.1801	
	N 1	0.1985	0.2161	0.2120	
	N 2	0.1757	0.1979	0.1930	
	N 3	0.1197	0.1379	0.1350	
Total $\chi 2$ / DF		3.62	7.11	6.98	0.21

In Fig. 5, the curves of the collection distances calculated with the conversion factor and coefficient *c* returned by the above Method D) are plotted against fluences. The original data points are also shown. In general the calculated curves are in good agreement with the data points.

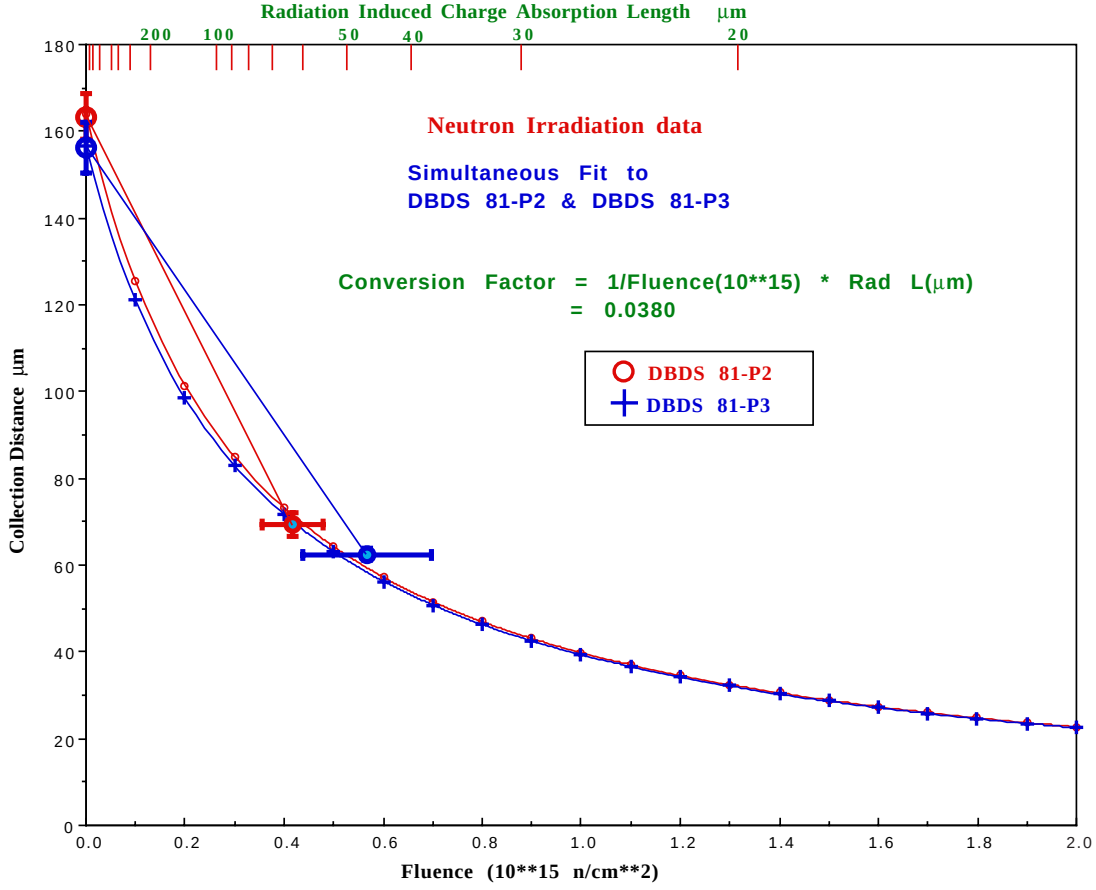

Fig. 5. Fit to DBDS 81-P2 neutron irradiation data.

The scale of the radiation induced absorption length is shown on the top of the graph. Based on such fit, the highest fluence point, 0.57 x 10^{15} n/cm^2, corresponds to the radiation induced charge absorption length of ~50 μm. The mean drift distance of electrons and holes is a half of the collection distance which is ~160 μm for these samples before irradiation. Therefore it is understandable that the additional charge absorption length of ~50 μm by irradiation reduced the signal slightly less than the half of the original signal.

An identical plot is shown in Fig. 6 for the method C). Though the fit of individual sample is not necessarily excellent, it is clearly seen that the general trend that large collection distances decrease fast with the increasing fluences whereas low collection distances withstand to higher fluences, is well reproduced. The conversion factor in this case translates the highest fluence points of U7 and N3, ~1.3 x 10^{15} n/cm^2, into ~30 μm in the charge absorption length.

Qualitatively such a trend is naturally expected from the *first principle* that the radiation effect is a creation of charge traps which *must be* uniform over the depth because it is the result of penetrating high energy particles. The relative fall off of the signal is a consequence of the two competing absorption processes, the pr-existed *linear* term and radiation-induced constant term. If the sample has a short average path length, either due to small thickness or due to small c-value, the effect of the radiation-induced absorption does not become comparable until the radiation-induced absorption length becomes much shorter. For those samples with greater collection distances, as a reflection of greater average path length either due to greater thickness or a better *c* -value, the radiation effect can be visible at lower fluence levels.

It is likely that there are no distinct differences between samples in terms of radiation hardness and the only relevant parameter that affects is the initial collection distance, or in other words, the average induced charge as the representative of the average path length of the signal charge. This is consistent with the observation in the general trend calculated in section 3.1.

Though a definitive conclusion awaits a greater data set especially on the samples of greater collection distances, we consider that the overall trend is well reproduced by the present model.

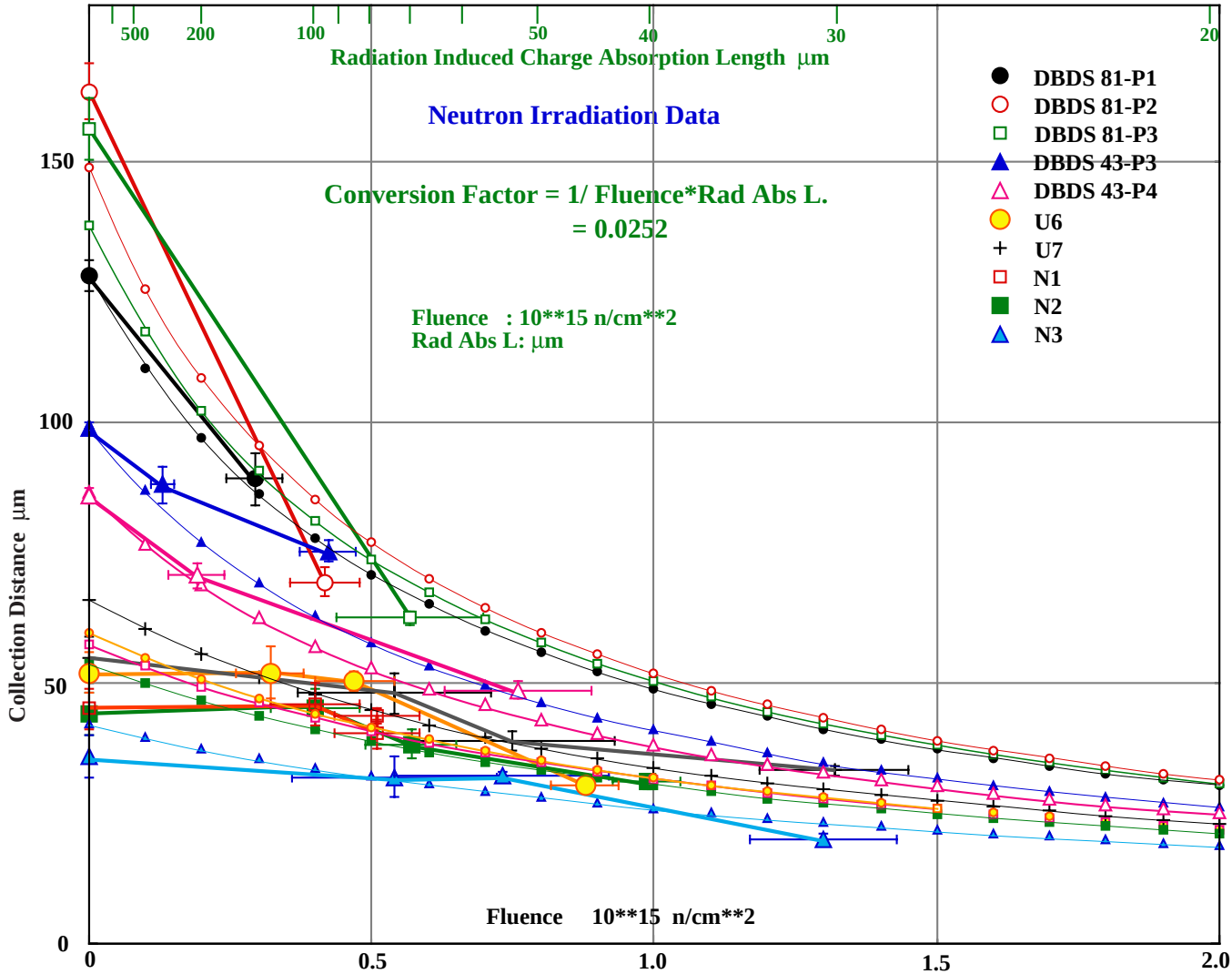

Fig. 6. Fit to all neutron irradiation data by the method C.

3.5 New neutron irradiaion data of the samples of high collection distances

A critical test of the validity of the present model would be a comparison with data of samples of large collection distance at low fluence to see whether the response drops rapidly at low level fluences as the model predicts.

In the recent meeting at SACLAY, R. Wedenig reported a new data points of neutron irradiation of the newest samples, D86 P1 and D86 P2 that exhibited high collection distance before irradiation. It showed a dramatic drop of the signal after exposed to rather low neutron fluence, 0.5 and 1 x 10^{14} n/cm^2 from the original collection distance of 225 and 206 μm, respectively.

It is a simple exercise to calculate such trend. Fig. 7 shows the calculated result overlaid on the original plot by R. Wedenig et. al.. Though the most of the collection distances in the new table have much larger, a factor ≤ 2, error bars than originallly shown, we simply use the same plots as in Fig. 6. Without knowing exact values of the collection distance nor the thickness and how it was lapped, we have arbitrarily taken 530 μm as the final thickness after lapping off the substrate side of as-grown 1 mm and 2 mm wafers corresponding to about a factor of two different values of the coefficient *c*. As expected the difference at any point up to 2 x 10^{15} n/cm^2 was less than ≤ 0.2 % for these significantly different parameters. Therefore a single curve for each of the samples is drawn from the zero-fluence point. As discussed in the previous section, this is another demonstration of the feature of the model that predict that the behavior of the signal decrease is almost *solely* dependent on the initial signal size, and once it is measured, the size of the signal can be calculated at any fluences. For comparison, curves for DBDS 81-P2 and DBDS 81-P3 are drawn. A conversion factor of 0.038 derived from those two old points was used.

The tendency of the fast drop at rather low fluence is well reproduced.

The straight lines connecting the data points in the original graph was merely to guide the eyes and there are no crossing among the calculated curves.

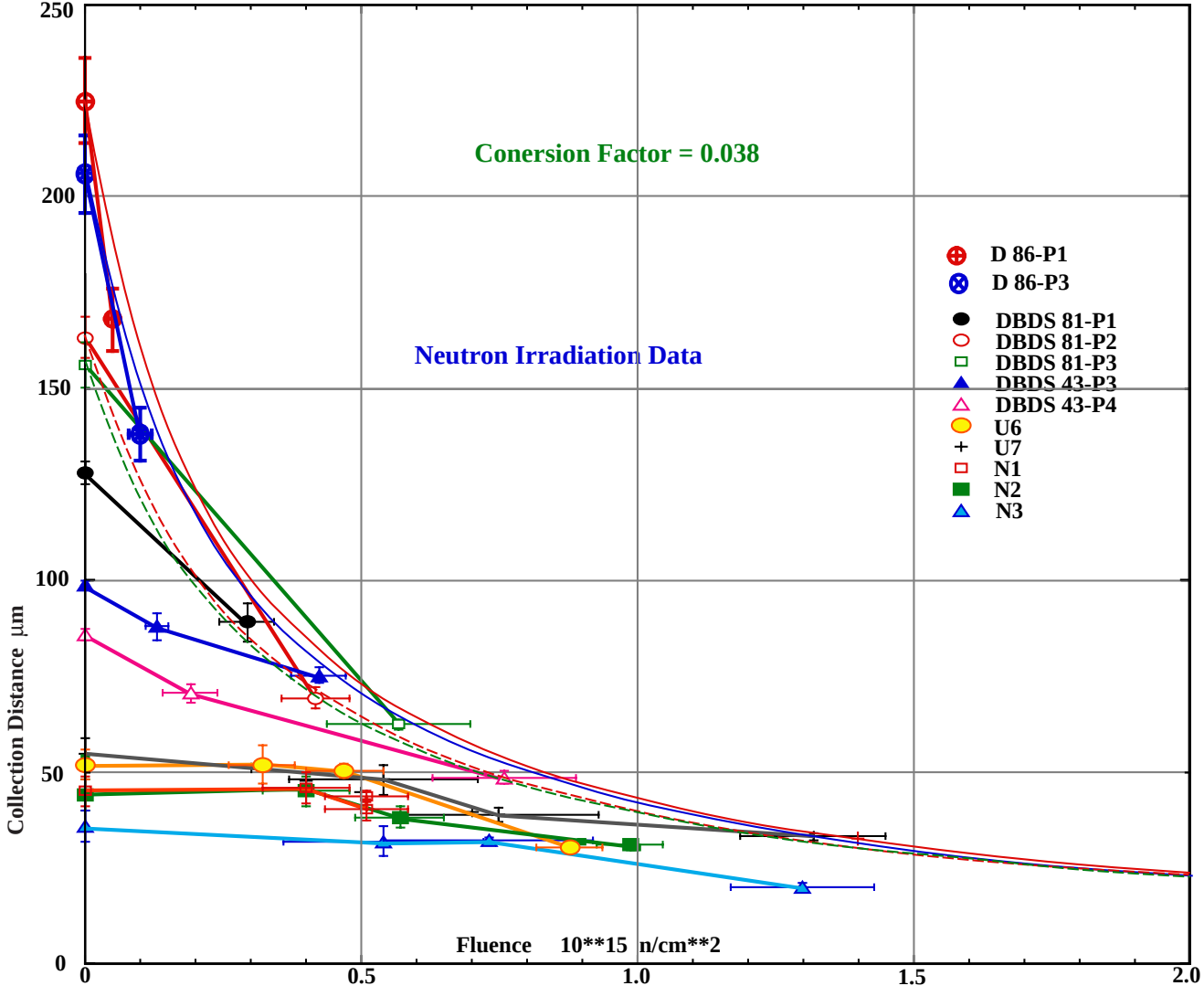

Fig. 7. Comparison with new data of the samples of high collection distances.

3.6 Comparison between pion irradiation and neutron irradiation

Comparing the fluence to $1/\lambda_{rad}$ conversion factor defined by (7), it is obvious that neutrons of ~ 1 MeV are about a factor of 4 to 5 more damaging than the pions of ~300 MeV/c which corresponds to the peak of 3-3 nucleon resonance.
However the real damage in LHC environment also depends on the expected flux of the particles. The following table is the flux read out from figures in CMS proposal[7] .

Table 4. Expected particle flux at CMS tracking cavity[7] .
(10 years)

Radius cm	z cm	Neutron $10^{14}/cm^2$	Charged Hadron $10^{15}/cm^2$
7.5	0	~2.4	~2.1
	100	~4.5	~2.2
11	0	~1.4	~1.1
	100	~2.5	~1.2
20	0	~0.8	~0.44
	100	~0.9	~0.5

Taking the composition of π^+, about 40 %, from the same proposal, the π^+ flux is about a factor of 3 to 4 times the neutron flux at z=0 cm. This ratio plus the contribution of other charged particles, more or less cancels out the difference in the damage per flux and therefore, neutrons and charged hadrons equally contribute to the damage in LHC environment. The rise of neutron flux at larger z is presumably due to the neutron cloud evaporated from the surface of the calorimeters and it is desirable to suppress such neutron component by hydrogenous absorber considering the greater effect of the damage by neutrons.

The conversion factor defined in (7) must be the reflection of relevant nuclear interaction cross sections because λ_{rad} must be inversely proportional to the density of the charge traps created by the radiation. The conversion factor from the overall fit for pion irradiation data is 0.00741 and that from neutron irradiation with Method C is 0.0252. If we take the Method D of Table 3, the value is 0.038. Since this is the fit to the two highest collection distance samples, it might be the most sensitive test while the overall fit is blurred by the less sensitive smaller collection distance samples.

The momentum of the π^+ beam for pion irradiation was 300 MeV/c corresponding to the top of Δ^{++} resonance formation. Without the luck of finding π^+ C cross section so far, we take π^+ D total cross section 259 mb[8], mostly elastic cross section, and multiply by 6 as the basis of π^+ C cross section. Taking nuclear shadowing effect factor of 0.9 as a guess, thanks to Jim Russ' suggestion, the cross section is 1.4 barn.

The energy of neutrons was above 10 keV and the n C total (=elastic) cross section ranges from ~2 to ~ 5 barn[9] in this energy range (See Table 5.). Based on the information from R. Wedenig that the spectrum was peaking at 1 MeV, we take 1 MeV as the average energy.

The ratio therefore is:

$$\text{Total cross section} : \frac{\sigma^{n}_{total}}{\sigma^{\pi+}_{total}} = \frac{2.6\ barn(1\ MeV)}{1.4\ barn} = 1.9.$$

whereas

Conversion factor : $\frac{f^{n}_{conversion}}{f^{\pi+}_{conversion}}$ = $\frac{0.0252 \sim 0.038}{0.0074}$

= 3.4 ~ 5.1 .

Therefore simple cross section alone cannot explain the difference between the effect of pions and neutrons. In addition to a better knowledge of true π^+ C cross section, understanding of the mechanism of creating charge traps and also the effect of recombination and or annealing are needed to clarify this argument.

It is an interesting exercise to calculate the density of charge traps assuming that every neutron scattered on a carbon nucleus creates one charge trap. Taking the total cross section of 2.6 barn, the carbon atom density of 1.7×10^{23} /cm^3*, and neutron fluence of 5×10^{14} neutrons/cm^2, one yields 2.5×10^{14} /cm^3 which is still negligible compared with the carbon atom density.

There is an experimental data[6] which is in line with such number. In the experiment, a diamond sample was irradiated by 1 MeV neutrons up to a fluence of 6 x 10^{14} n/cm^2 and then examined by cathodeluminescence spectroscopy. As a result, concentration of 1 x 10^{14} /cm^3 was found as the vacancies that corresponds to GR1 line which was absent before the irradiation. Therefore the corresponding cross section is 0.88 barn. This number is a factor of ~3 smaller than the density calculated from the cross section but considering a possible effect of recombination or annealing the two numbers are not too far from each other.

As an additional note, it should be pointed out that such charge trap density corresponds to 53 ~ 79 μm as the absorption length using the conversion factor we have derived. If the charge traps corresponding to the preexisting linear term absorption are of similar nature, we can extrapolate the above number to estimate the density to be on the same order of magnitude, a few x 10^{14}/cm^3. This is because the collection distance of ~200 μm is equivalent to the charge absorption length of ~100 μm due to the fact that electrons and holes are contributing almost equally.

As a conclusion, the ratio of the total cross section does not explain the difference between the damage by π^+ 's and neutrons. Neutrons are far more damaging than π^+ if one only considers the total cross section.

Table 5: Total neutron - carbon cross section from "Neutron cross Section".

Beam energy MeV	Cross section barn	
0.01	4.8	
0.02	4.7	
0.05	4.6	
0.1	4.5	
0.2	4.3	
0.5	3.3	
1	2.6	
2	1.7	
2.1	4.2	(Sharp peak)
2.1 ~ 5		(Structure)
5	1.2	

* Note: Density=3.51 g/cm^3, Atomic weight of carbon=12.011, Avogadro No. = 6.022x1023/mol

4. PULSE HEIGHT DISTRIBUTION

4.1 Motivation for study

Since the pulse height distributions for the samples before and after pion irradiation were first presented two years ago, it has been puzzling why it appeared as if the distribution after irradiation has lost high pulse height portion whereas the lower end of the distribution does not seem to have changed much. Similar distributions have been presented for the case of neutron irradiation. If it is the case, the implication is that the detection efficiency, which is dependent on the lower tail of the distribution, should be affected less.

In order to study such questions, we have taken the pulse height distributions of DBDS 81-P2 before and after neutron irradiation up to 4.17×10^{14} n/cm^2 presented by R. Wedenig. We have scanned the presented graphs for the comparison with the calculated results. In fact, by comparing the spectra before and after the irradiation, it is apparent that the distribution after the irradiation is not only lower in general but also much *narrower* in respective scale than the distribution before the irradiation.

4.2 Model formulation

Taking the previously described fit with Method D), the fluence-to-absorption length conversion factor is $0.038 \{ (10^{15}$ neutrons/cm$^2) \bullet \mu m \}^{-1}$ and therefore the above fluence corresponds to 63.11 μm as the charge absorption length.

The method of calculating the pulse height distribution is as follows: We divide the total thickness of the diamond sample into multiple equal thickness slices and, for each event of minimum ionizing particles (MIP), we generate slice-by-slice pulse height and sum up as the pulse height for a MIP. We used the random number generator RANLAN in CERNLIB[9] to generate the Landau distribution for slice-by-slice pulse height. For each slice, the average transmission distance of the generated electrons (holes) was calculated based on the previously described formula (5). The product of the number of electrons (holes) and the transmission distance, normalized by the total thickness, is taken as the induced charge. The induced charges for each of the slices are then added together to form the pulse height for each event of MIP's passing through the entire thickness.

The input parameters are the following:

- Nominal *average* energy deposit onto a slice using the nominal density of diamond, 3.5 g/cm^3, and dE/dx, 1.745 MeV / (g/cm^2).
- The energy deposit is converted to the number of *e-h* pairs using canonical electron-hole pair creation energy 13 eV.
- The preexisting *linear* absorption coefficient *c* of 0.1106 as derived from the measured collection distance of the unirradiated sample as listed in Table2 before.
- Radiation induced charge absorption length λ_{rad} of 1 m for un-irradiated sample and 63.11 μm for irradiated sample.
- Equal contributions from electrons and holes were assumed.

It was found that once the energy deposit is properly integrated within each slice as described by the formula (6), the total pulse height distribution is not dependent on the number of slices at least within the range of single slice up to 200 slices. Examples of the calculation with λ_{rad} =1 m as the input parameter is shown in Fig. 8.

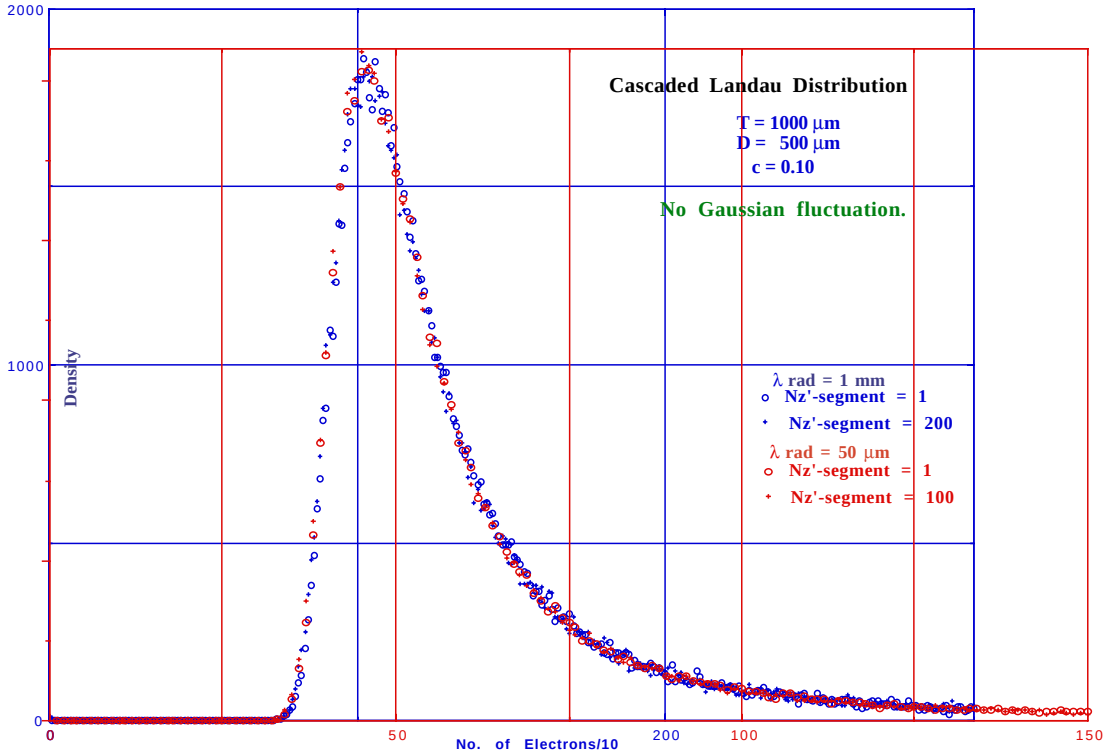

Fig. 8. Cascaded Landau distribution without any fluctuation. Distribution after irradiation (λ_{rad} = 50 μm) is overlaid on the unirradiated distribution (λ_{rad} = 1 m) with horizontal scale normalized to match the peak.

The results of different numbers of slices exactly overlay with each other. This is presumably due to the built-in cascading process in the Landau distribution itself. The pulse height distribution thus calculated is much narrower than the measured pulse height distribution before the irradiation.

Also shown is the result calculated for an arbitrarily chosen λ_{rad} of 50 μm. Adjusting the horizontal scale of the induced charge, the result for λ_{rad} =50 μm can be exactly overlaid on the spectrum for λ_{rad} =1 m. It is clear that the distribution without fluctuation of the parameters does not change the *shape* of the spectrum. The pulse height scale alone is reduced due to radiation damage.

It is imaginable that the real pulse height distribution is much broadened due to local inhomogeneity of the transmission due to the crystalline structure of diamond within the finite area of the exposure to the beam which may not be represented by a single value of the coefficient *c*. Therefore first we have introduced a fluctuation of the values of the coefficient *c* with a multiplicative factor of Gaussian shape centered at unity. Furthermore the scale of the positive side of the Gaussian distribution, or in other words, the σ of the Gaussian distribution, was scaled by a factor given as an input. The explicit formula is as follows:

$$c = \left[1 + a \bullet Scale \bullet x_c\right] \bullet c_0$$

where a_c : an factor equivalent to σ of Gaussian distribution

Scale : a scale factor to provide a wider positive side distribution

$$Scale_c = 1 \qquad x_c \le 0$$

$= \quad Scale_c^{+} \quad 0 \le x_c$,

x_c : a variable that fluctuates with Gaussian frequency.

$$f_c = \frac{1}{\sqrt{2\pi}} \exp\left(-\frac{1}{2} x_c^2\right)$$

c_0 : Central value of c.

We limited the range of x_c as

$-3 \le x_c \le 3$.

The fluctuation was applied on event-by-event basis. Such fluctuation of the value of c might be realistic considering the random polycrystalline structure of CVD diamond whose local transmission can vary in a certain range. The different scale factor for negative side and positive side fluctuation is justifiable considering that the poor transmission is bound by zero whereas the good transmission could be extended to larger values.

The result of introducing such Gaussian fluctuation of c did not emulate well the shape of the observed pulse height distribution especially at the lower pulse height tail extending to zero. Therefore we further applied a multiplicative Gaussian shape factor to the final pulse height distribution.

$$Q_{induced}^{final} = \left[1 + a_Q \cdot x_Q\right] \bullet Q_{induced}^{cascaded} .$$

where x_Q : a variable that fluctuates with Gaussian frequency

a_Q : a factor equivalent to Gaussian σ.

We limited the range of x_Q as

$-3 \le x_Q \le 3$.

It should be noted that he observed spread of the pedestal peak is supposed to represent the final noise in the experimental setup and it was much narrower than the spread needed to explain the observed distribution. Other possible justification is the often reported gross local nonuniformity. Since the fluctuation of the value of c was event-by-event basis, such fluctuation on the final induced charge can take care of the possible local fluctuation of c along the track of each event.

Fig. 9 demonstrates the effect of Gaussian fluctuation using the parameters for the DBDS 81-P2 as an example. Spectra with fluctuation of the value of c with *scale*(+) =1, 2, and 3, and the final induced charge are compared with the spectrum without any fluctuation in Fig. 9a. The input parameters are the same as the final set adjusted for DBDS 81-P2. It is obvious that the effect is to make the spectrum wider without changing the most probable peak. Then the spectrum of λ_{rad}= 50 μm was calculated by simply switching the value of λ_{rad} leaving all other parameters unchanged as shown in Fig. 9b. Only the scale factor of 3 is plotted to be compared with the spectrum without fluctuation. For comparison, the spectra for λ_{rad}= 1 m is overlaidwith the horizontal scale adjusted to have exact overlay of the un-fluctuated spectra same as Fig. 8. It is apparent that the fluctuation is the cause of the relative narrowing of the *shape* after irradiation.

If there is no fluctuation, or, in other words, nonuniformity, the spread of the pulse height is only due to Landau fluctuation which is not affected by the radiation damage. The radiation damage only changes the overall pulse height.

Also it should be reminded that the fluctuation of the coefficient c is event by event basis. Therefore, by introducing the fluctuation of c, events of large *average* pulse height are mixed with those with small average pulse height representing local nonuniformity. The high c -value component decreases more than low c-value component in the relative scale, as reproduced in the previous sections, and, as a result, high pulse height portion of the spectrum shrinks more changing the *shape* of the spectrum.

In Table 6, the average charge is tabulated for each of the spectra in Fig. 9 a. The average charge is not too far off from the measured value for any of the parameter sets.

Table 6. Average charge for spectra with different parameters.

Parameter set	$< Q_{\leq 20000\ e} >$	$Q_{Calc}>/<Q_{Meas}>$
Measured	5883 e	
Calculated		
No fluctuation.	5862 e	- 0.4 %
Gaussian fluctuation. ($a_c = 0.7$, $a_Q = 0.85$)		
$Scale_c^+ = 1$	5719 e	- 2.8 %
$Scale_c^+ = 2$	6071 e	+3.2 %
$Scale_c^+ = 3$	6368 e	+ 8.2 %

Again the calculation was made for both directions of the motion of the deposited charges with respect to the direction of the "linear" growth of the transmission. Since there was no difference in the pulse height ditribution between the results for opposite direction of the motion, the induced charge calculated for one direction was simply doubled to represent the added charges induced by the motion of electrons and holes.

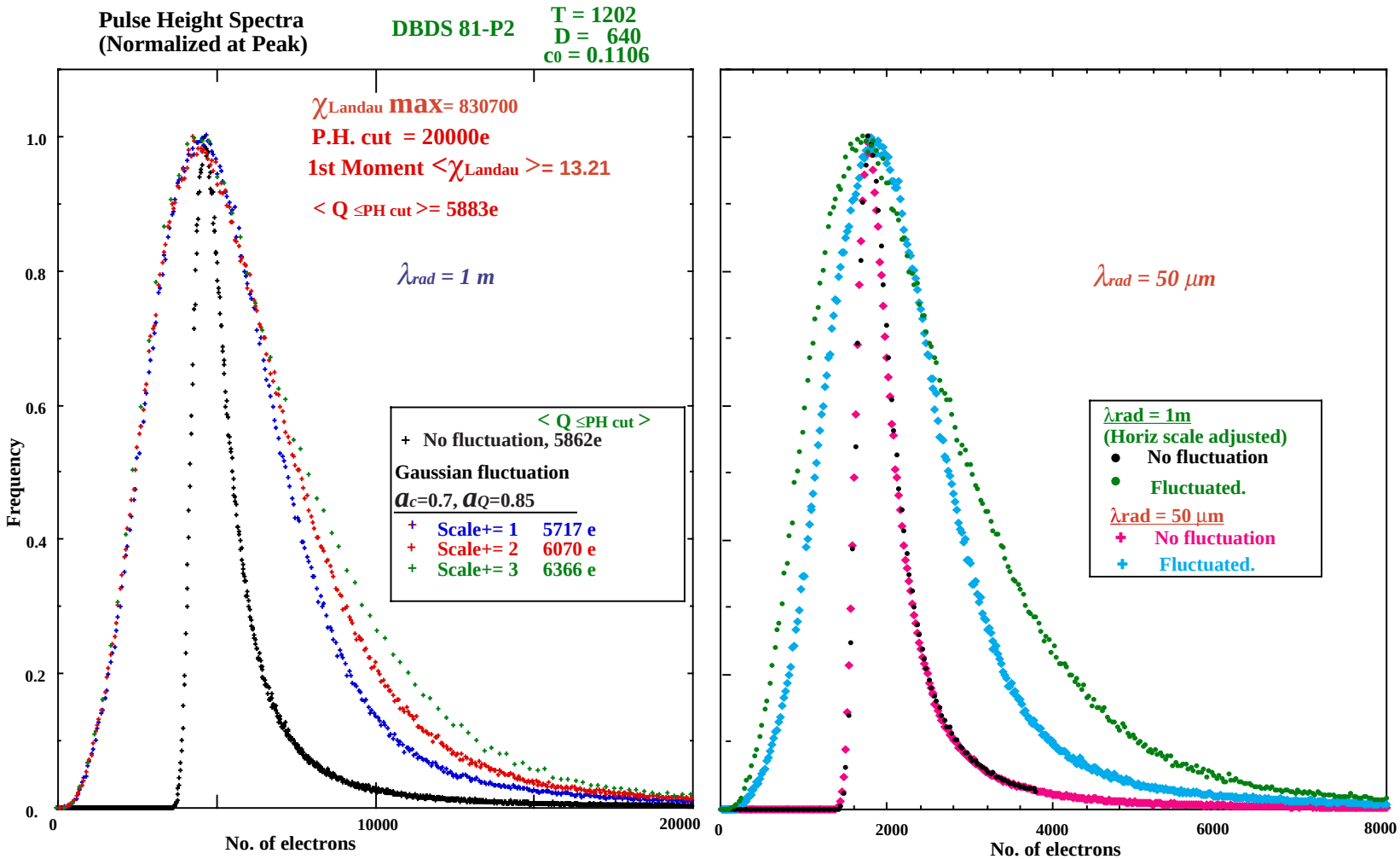

a. Spectra before irradiation corresponding to λrad = 1 m. b. Spectra after irradiation corresponding to λrad = 50 μm.

Fig. 9. Effect of Gaussian fluctuation of coefficient *c* and the final induced charge.

4.3 Neutron irradiation data of DBDS 81-P2

We now apply the model developed in the previous section to the data of DBDS 81-P2. As demonstrated in Fig. 9, the position of the most probable peak is automatically determined and the only adjustable parameters are the "fattening" parameters that represent the fluctuation.

After visually seeking plausible fit, a set of values of the parameters

a_c = 0.7
$Scale_c^+$ = 3
a_Q = 0.85

seemed to give a reasonable fit to the measured spectrum of the un-irradiated sample with the input parameter λ_{rad} of 1 m. The result for the final set of parameters is overlaid on top of the measured pulse height spectra in Fig. 10. Fig. 10*a* is the distribution before the irradiation and *b* is the one after the irradiation corresponding to λ_{rad} = 63.11 μm.

The shape of the distributions are reasonably well emulated both of the measured spectra. The average charges of the spectra were calculated, as tabulated in Table 7, applying different cut on each of the spectra, 2000*e* for the spectrum before the irradiation and 9000*e* for the one after the irradiation. The former is what was in the original measured spectrum and latter corresponds to the effective cut implicitly applied by the limited statistics due to which no event was accumulated beyond ~9000e.

Table 7. Comparison of the average charge.

Neutron Fluence 10^{14} n/cm^2	Measured Collection dist.	<Q>	Calculated P.H. cut	<Q>	$<Q_{Calc}>/<Q_{Meas}>$
Before irradiation	163.42±5.34	5883e	20000e	6368e	1.082
4.17	69.41±2.69	2499e	9000e	2603e	1.042

For a comparison, the distribution for an arbitrarily picked λ_{rad} = 80 μm (conversion factor 0.030) is plotted in Fig 11.

A note should be added on the issue of the cut-off of the distribution. In calculating Landau distribution, there are questions on what the cut off should be for several variables and what value should be used as the electron-hole pair creation energy $E_{e\text{-}h\ pair}$. The Landau distribution that descries the fluctuation of the energy deposit around the *average* value, is based on a universal Landau function as a function of dimensionless Landau variable x_L which is then converted into energy by a factor with a dimension of energy. The universal Landau function has a long tail extending to infinity although the major portion of the distribution is within small values of x_L (95% is below x_L = 23.) starting from $x_L \approx$-2.5. In order to make the average of the distribution zero as it supposed to be, the cut-off needs to be an extremely high maximum value of the variable (~10^6). It turned out that if such canonical set of the parameters for Landau distribution are used, the observed average charge was well reproduced. The calculated average charge was off by only 8.2 % from the measured average charge for the unirradiated sample and 4.2 % for the irradiated sample as listed in Table 7.

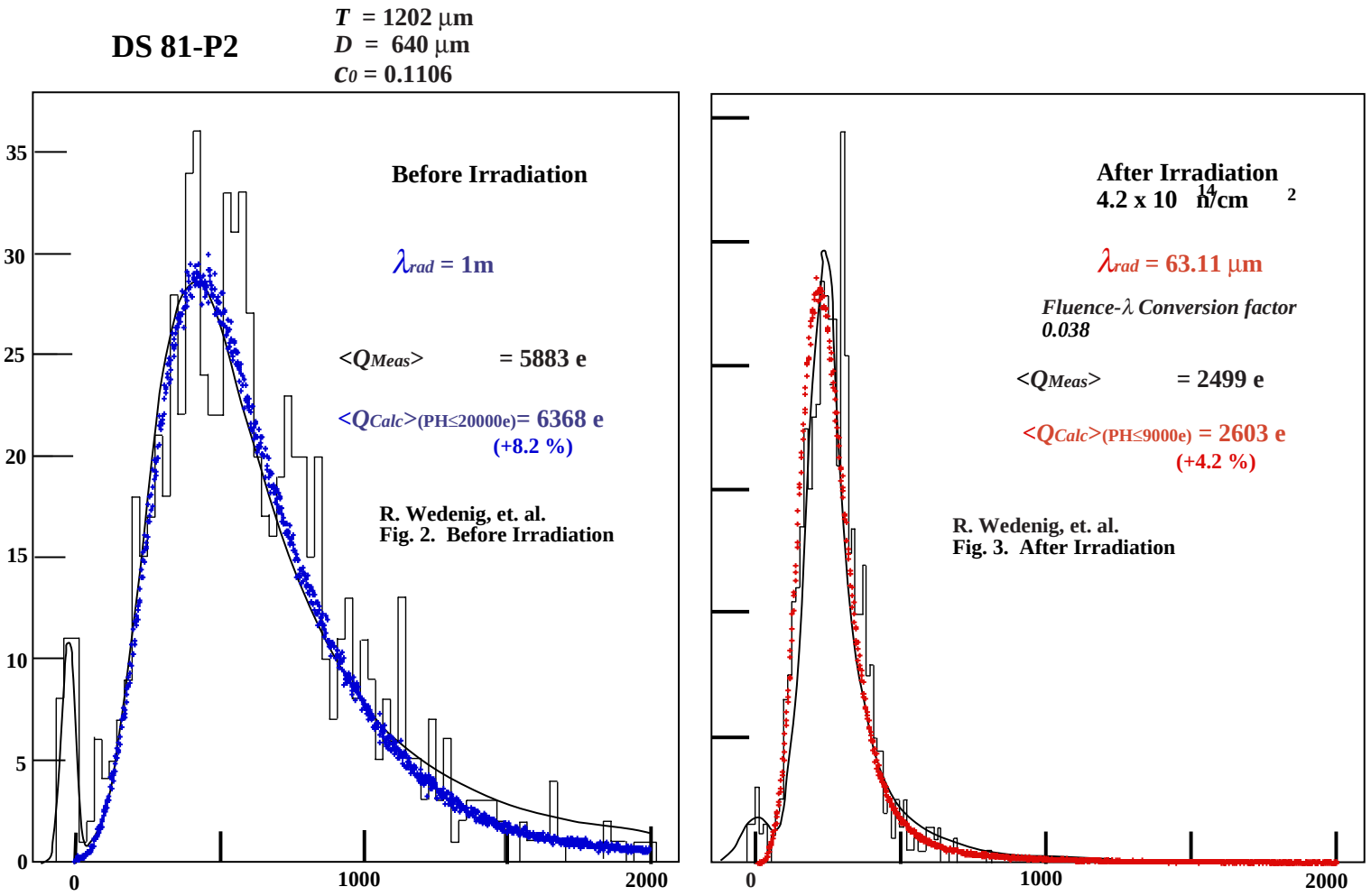

(a) Unirradiated. (b) After irradiated by total fluence of 0.42 x 1015 neutron/cm2.

Fig 10. Simulated DBDS 81-P2 pulse height distribution by cascading Landau distribution.
The background histograms are scanned from the graphs of R. Wedenig, et. al..

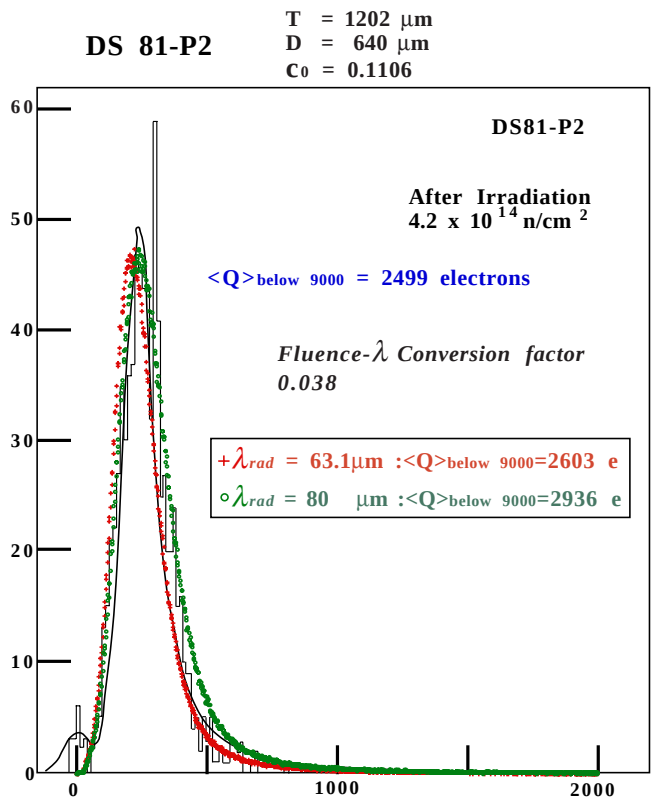

Fig. 11. Fit to the spectrum after irradiation. λ_{rad}=63 μm is based on the fluence to λ_{rad} conversion factor of 0.038 derived from the fit to DBDS 81-P2 and P3 as shown in Fig. 5 and λ_{rad}=80 μm corresponds to the conversion factor of 0.030.

It should be re-emphasized that the parameter set used in the calculation was:

a) canonical maximum value of the Landau variable.
b) first moment calculated for the above cutoff using XM1LAN program as the average energy deposit.
c) nominal $E_{e\text{-}h\ pair}$ 13 eVcorresponding to 47 *e-h* pairs/μm.
d) experimental cut on pulse height at 20000 electrons for unirradiated sample.
e) experimental cut on pulse height at 9000 electrons for irradiated sample corresponding to the effective cutoff due to the limited statistics of the data.

In the calculation, 0.1106 was used for the coefficient *c* which was derived from the observed signal using empirical 36 *e-h* pair per μm times the measured collection distance. This value corresponds to $E_{e\text{-}h\ pair}$ of 17 eV. Therefore the fact that the observed signal was reproduced using nominal 13 eV as $E_{e\text{-}h\ pair}$ indicates that the empirical $E_{e\text{-}h\ pair}$ of 17 eV is merely a result of the experimental cut on the final pulse height distribution applied on purpose or implicitly due to the finite dynamic range of the system and also depending on the finite statistics. Also probable escape of the high energy δ-rays must be contributing to the loss between the deposited energy and the number of e-h pairs created.

It should be reminded that the model assumed equal contributions from electrons and holes. The good agreement in the final average charge is another support for the above assumption though not conclusive.

4.4 Pulse height spectra of newer samples with large collection distances

There have been reports that the pulse height distribution of the latest samples are much improved resulting in the ratio of the FWHM and the most probable peak is around unity. The ratio used to be much larger, ~2. It is interesting to simulate those newer samples in view of the present model.

We examine the pulse height distribution of CDS 61 and CDS 62 reported in "Report on DeBeers Sample, No. 5/98". Comparing these with the spectra of other samples in the Report No.1 / 99, These two seems to be among the very best so far.

We scanned the graphs based on CERN measurement in Graphs. 3 and 4, for CDS61 and CDS 62, respectively and tried to tune the parameters of the calculation visually.

As discussed in the previous section, the parameters we float are those for "fattening" the spectra but not the intrinsic parameters.

Since the pedestal peak is clear in Fig. 3 of the Report, we added a randomly generated noise term of Gaussian distribution to the final spectra. The pedestal peak in Fig. 3 of the Report was well reproduced by a $\sigma = 350\ e$ which was used both for the CDS 61 and CDS 62.

First the linear term coefficient *c*'s were derived from the measured charge for which we used the mean charge shown in the insets in the graphs instead of the collection distances, tabulated in the table in the same report, times the empirical number of *e--h* pairs per unit length, 36 *e-h* / μm which result in slightly different numbers. Since we did not find the as-grown thickness of the samples, we arbitrarily used 1 mm and 2 mm and calculated the values of c for each of the thickness which naturally about a factor of two different. The spectra were calculated for the two combinations of the as-grown thickness and the coefficient c but the results were indistinguishable from each other again demonstrating that the spectra are only dependent on the amount of the charge.

As before, the energy deposit and the *e-h* creation energy used in the calculation are the nominal values, 1.745 MeV/ (g/cm^2) and 13 eV/*e-h* pair, respectively and the nominal maximum of the Landau variable were used. On the final spectra, the experimental cut, 20000*e* and 30000*e* were applied to obtain the average charges for CDS61 and CDS 62, respectively.

In Figs. 12 and 13, the fitted spectra are overlaid on the original spectra.

It should be noted again that the most probable peak is automatically reproduced in good agreement with the observed spectra independent of the "fattening" parameters.

Good agreement of the average charges between the measured and the calculated values are obtained. The "fattening" parameters are about the same for both of the spectra.

Table 7 summarizes the parameters of the fit. Only the results for assumed as-grown thickness of 2000 μm are shown.

The major difference between the parameter set for the previously examined DBDS 81-P2 in section 4.3 and these newer samples, CDS 61 and 62, is the Gaussian fluctuation factor for the coefficient *c* which is much smaller for the newer samples consistent with the observation that the spectra are much narrower.

To illustrate the feature of these parameters, distributions for CDS 62 with and without the fluctuation are compared in Fig. 14. The most probable peak is essentially the same. For a comparison, also plotted is the distribution for the material of the same thickness, 535 μm, with infinite transmission. Fluctuation is not included. The difference, about a factor of 2, in the average charge is the difference between the average drift distance of 535 / 2 = 267.5 μm for infinite transmission and the measured average drift distance which is the half of the measured collection distance 243 μm.

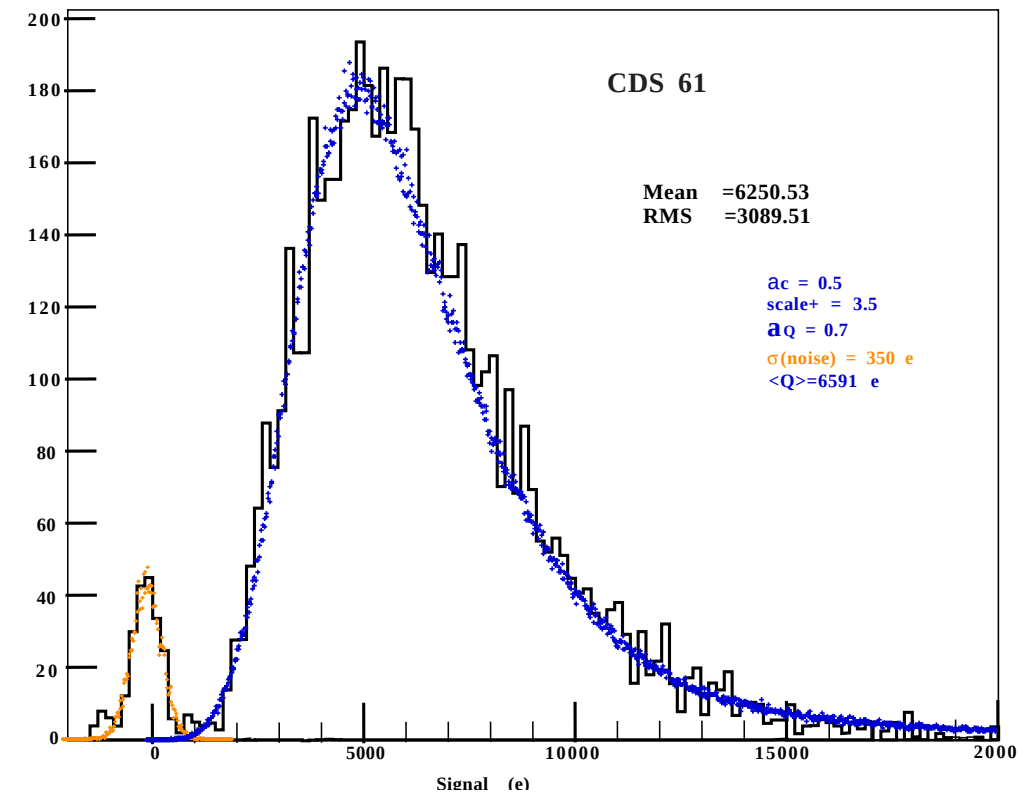

Fig. 12. CDS 61 pulse height distribution.

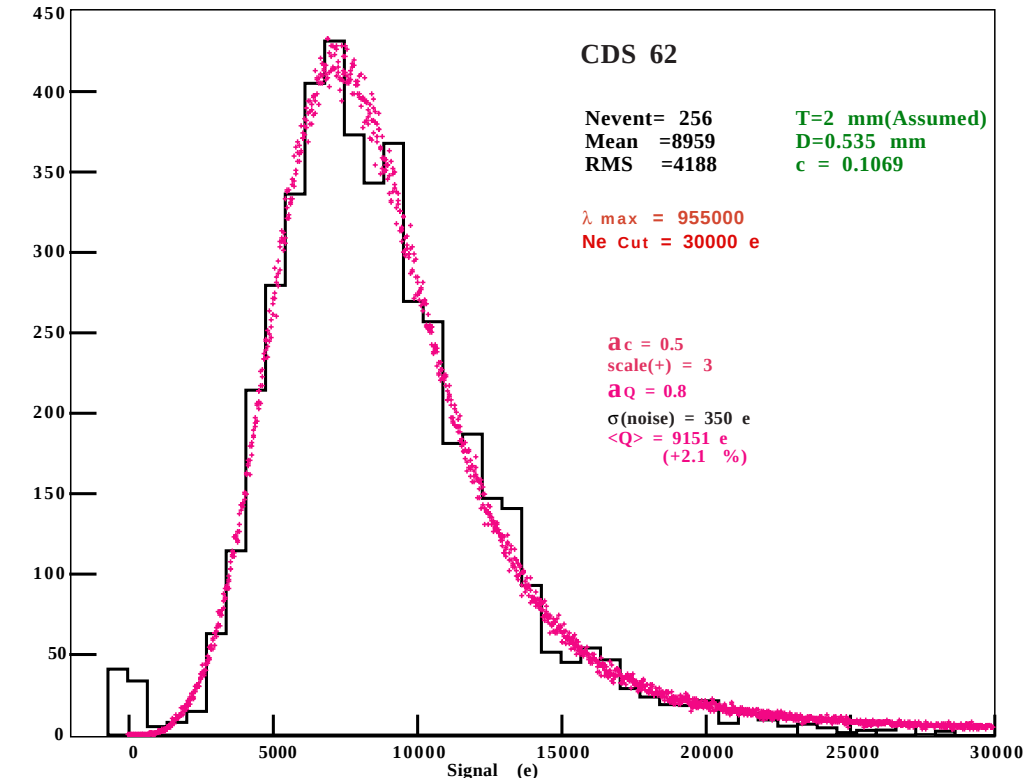

Fig. 13. CDS 62 pulse height distribution.

Table 8. Parameters of the fit to CDS 61 and CDS 62.

	D µm	*T* µm	*c*	Cut_{Meas}	$< Q_{Meas} >$	$< Q_{Calc} >$	$Q_{Calc}/<Q_{Meas}>$
CDS 61	521	2000 (Assumed)	0.06325	20000*e*	6250.53 *e*	6591 *e*	+5.5 %
Gaussian fluctuation parameters : $a_c = 0.5$, $Scale_c^+ = 3.5$ $a_Q = 0.7$ $\sigma_{Noise} = 350\ e$							
CDS 62	535	2000 (Assumed)	0.1069	30000*e*	8959.32 *e*	9151 *e*	+2.1 %
Gaussian fluctuation parameters : $a_c = 0.5$, $Scale_c^+ = 3$ $a_Q = 0.8$ $\sigma_{Noise} = 350\ e$							

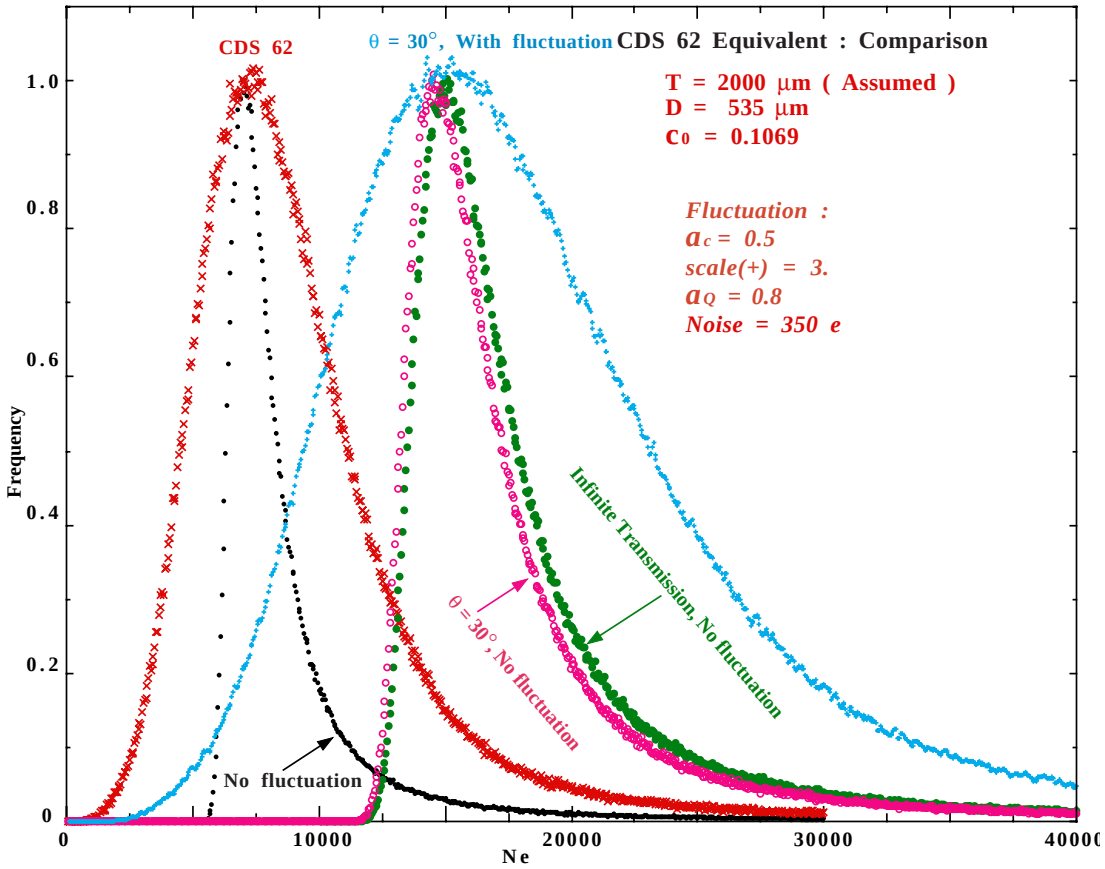

Fig. 14. Comparison of the CDS 62 equivalent spectra with and without fluctuation and for infinite transmission. Spectra for 30° incidence is also plotted.

4.5 Effect of the incident angle

If the particles are incident on the diamond layer with an angle instead of the normal incidence, the energy deposit is larger without changing the total drift distance. This is the case for the particles from interaction point in a collider environment except for 90° in the polar angle assuming that the vertex detctor is cylindrically arranged around the beam axis. The effect on the induced charge is equivalent to have a denser material with the same geometry and the enhancement factor is expected to be $1/\sin\theta$ with θ being the polar angle angle. As an example, the spectra for a track of 30° in polar angle is overlaid in Fig. 14. Presumably the effect of the non-uniformity is the same as the normal incidence and therefore the same parameter set for CDS 62 was used. Also shown is the distribution without fluctuation which is about the same as the spectra for infinite transmission with normal incidence. Since the effect is only to change the energy deposit whereas the broadening of the spectrum is due to the non-uniformity of the transmission which is independent of the incident angle, the spectrum was simply stretched in the horizontal scale by a factor of 2 as expected from the argument above. This is a speculation guided from the assumption of how the non-uniformity is caused and needs experimental verification.

The effect of the radiation damage is the same as the normal incidence using the same argument in the above. However, since the pulse height is stretched, the threshold can be much higher for the same detection efficiency, as discussed later. Conversely, one can reduce the thickness of the material in the forward angles with the same pulse height as the thicker material in the central region. Then, with reduced gap thickness, it is more tolerant against the radiation damage.

To conclude, the angular effect is significantly positive in the forward angles.

As long as the strips or pixels are long in the direction of *z*- axis and the radius of the diamond layer with respect to the beam axis, the r-φ resolution does not change with the angle in the first order.

4.6 Possible double layer configuration

In general, two thinner layers instead of a single thicker layer are stronger against radiation damage because of the smaller average drift distance, as discussed before. In Fig. 15, a spectrum of such double layer detector is compared with a single layer spectrum with the parameter set of CDS 62.

The double layer detector is taken as an event-by-event convoluted sum of two layers each of the half, 267.5 μm, of the original 535 μm cut out from 1000 μm material with the same value of the coefficient *c*, 0.1069. Presumably the coefficient *c* is the representative parameter of the growth process and therefore the cost of such double layer must be about the same as the single layer cut out from twice thick grown material. Though the diode capacitance is quadrupled, overall capacitance that affects the noise is dominated by the intrer-strip capacitance which is about doubled. Therefore the noise was doubled in the calculation.

It is seen in this figure that the most probable peaks are at the same pulse height and only the width changes. Though the spectrum for the double layer is narrower because of the range of the linear growth of absorption length in the thinner layers is small, it depends on how the parameter fluctuates and this is not meant to emphasize the difference. However, although the average charge is essentially the same, the radiation damage effect is slightly different as discussed in the next section.

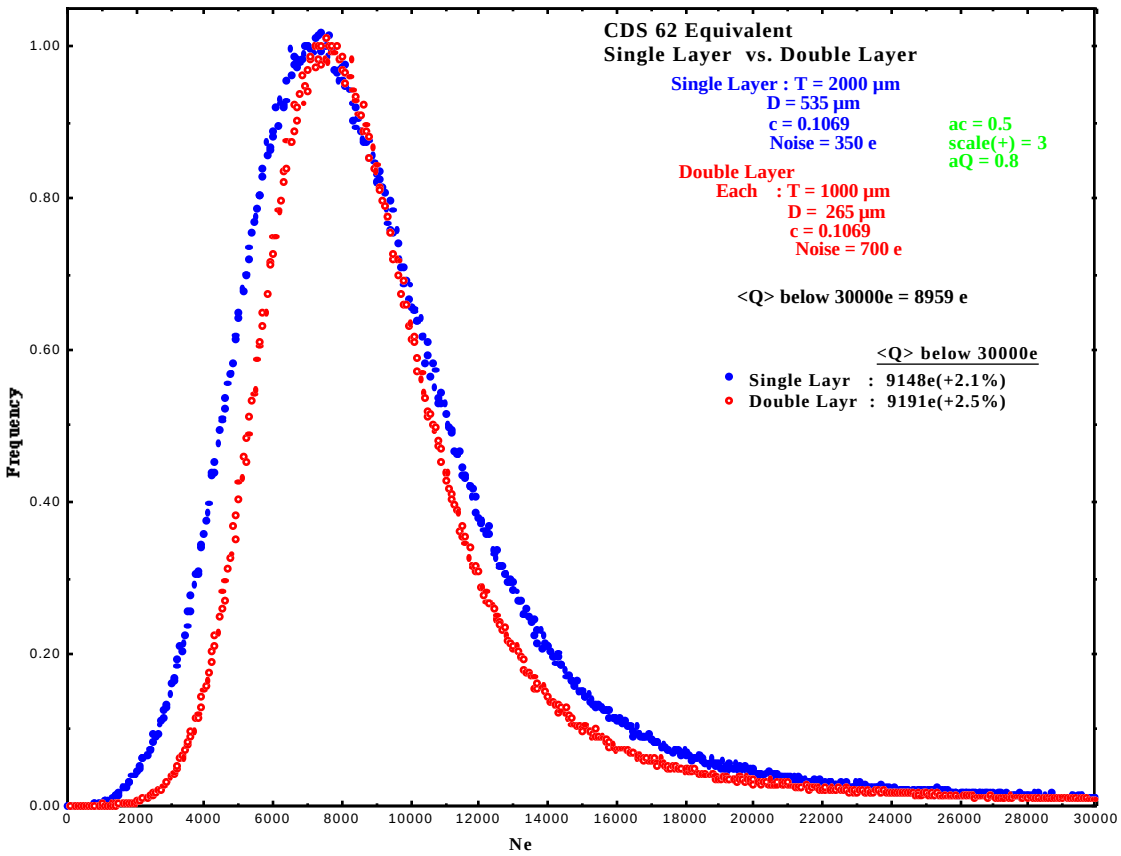

Fig. 15. Spectra of CDS 62 equivalent single layer and double layer detectors.

4.6 Implication to the detection efficiency

Since the calculated distribution reproduces the measured distribution at the lower side tail reasonably well, we can infer the detection efficiency for various fluence of irradiation using the same parameter set of CDS 62. It should be pointed out that though this sample is the best in terms of the signal size with good pulse height spectrum, the value of *c*, even assuming the as-grown thickness of 1 mm, is not exceptional and if the as-grown thickness is 2 mm, the value of *c* is in the rather smaller class.

In Fig. 16, curves for the threshold induced charges corresponding to the efficiencies of 99 %, 98 %, and 95 % are plotted against neutron fluences for three different examples. Three empty symbols are for the simulated CDS 62 with the set of parameters found in the previous section assuming that the as-grown thickness is 2 mm. As in Fig. 13, noise of Gaussian distribution of a sigma of 350*e* is convoluted. As a reference, curves of zero-fluctuation are also plotted. These curves are supposed to be the the upper limit for a sample with this amount of average induced charge. A third group of curves are for a double layer configuration with each layer exactly the half of the original thickness of CDS 62. Two 267.5 µm thick layers were each assumed to be cut out from as-grown thickness of 1000 µm with the same value of *c* as the CDS 62. The signals from each layer are convoluted event-by-event corresponding to strip-by-strip ganging.

As discussed before, the decrease of the efficiency for higher radiation dose is slower than single layer case due to the fact that the charge only travels 200 µm at most in each of the independent layers. The efficiency at lower dose is somewhat artificial because it depends on the detail of the fluctuation parameters. However, the trend in higher dose is

real because of the shift of the average pulse height is obvious due to the previously discussed reason.

Thus double layer of half thick pieces is potentially an advantageous option, both signal wise and economically, if the technique to lap diamond material to ≤300 μm is practical. .

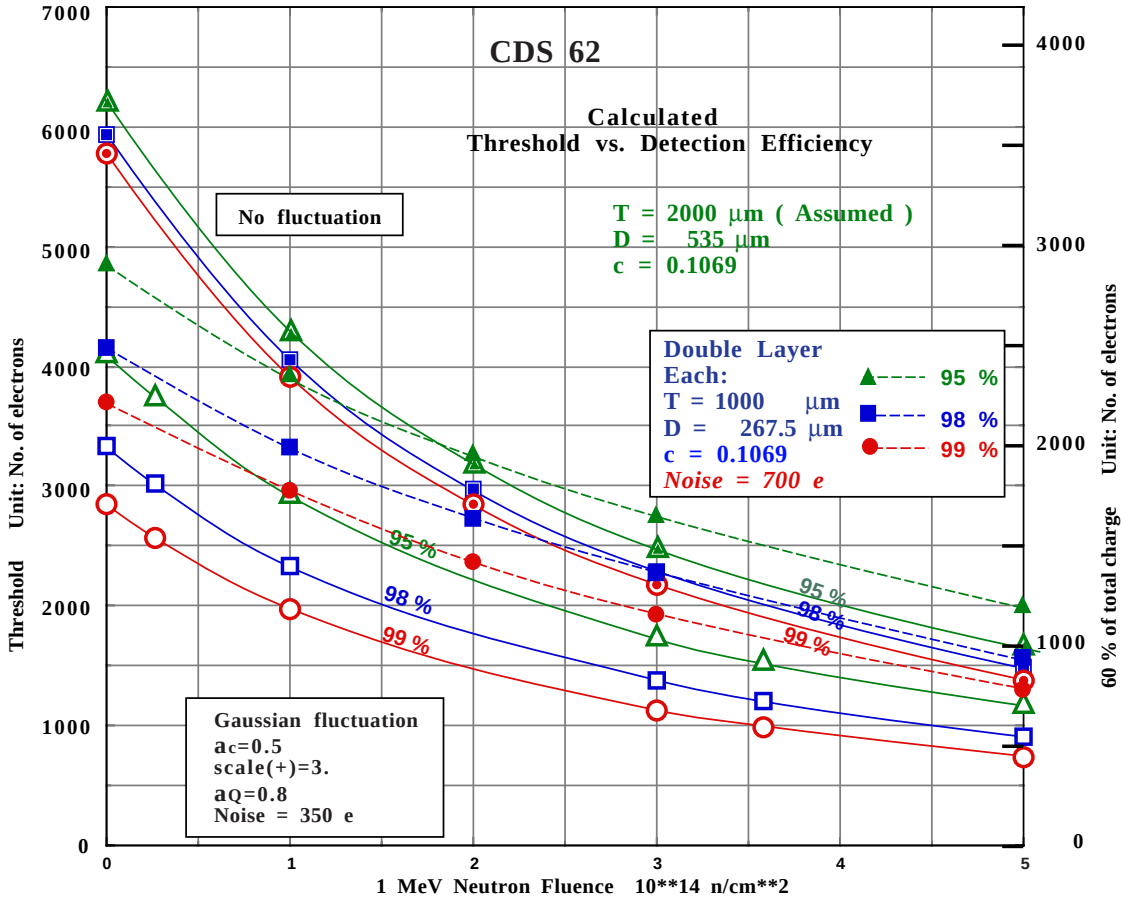

Fig. 16. The vertical axis is the threshold in the unit of the number of electrons. Scale for the 60 % of the total charge is shown on the right hand side axis as a scale for the case in which 60 % of charge is collected to a single central strip.

Another possibility for a double layer configuration is not to make strip-by-strip ganging but to measure each layer independently at the lower level trigger, i.e., to make a trigger as an OR of the two layers. In this case low detection efficiency for each layer, for example 90 % (85 %), still gives a high enough efficiency, 99 % (98 %), for the OR-ed trigger. Fig. 17 shows the efficiency of 267.5 μm layer. Noise of 350 *e* , as measured for CDS 62, was convoluted.

It should be noted that in such configuration, each layer can be double sided.

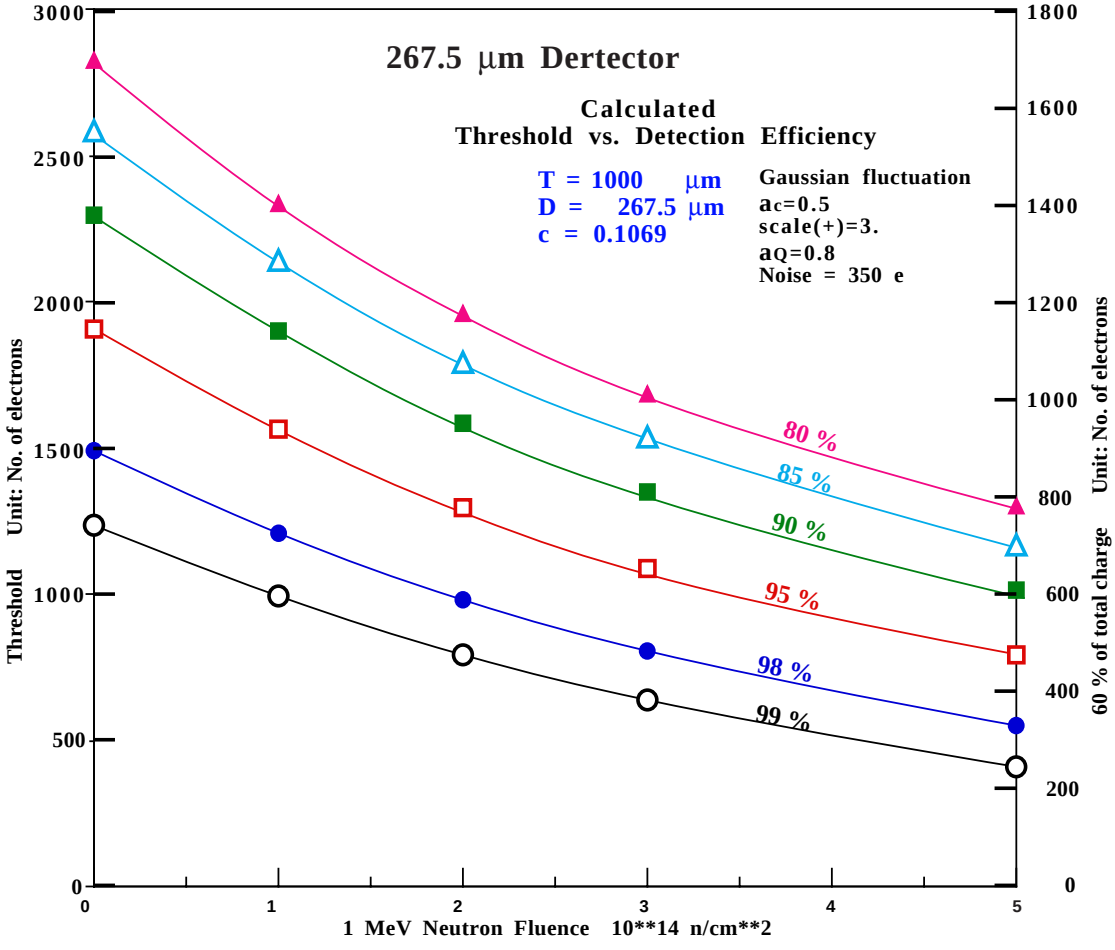

Fig. 17. Threshold charge vs. neutron fluence for various detection efficiencies of 267.5 μm thick layer.

As discussed before, the path length of the particles significantly increases in the forward angles and the size of the signal increases by the same factor while the radiation damage effect is the same as the central region with normal incidence. Therefore the detection efficiency significantly benefits from going into forward angles.

In Fig. 18, the threshold charge for various detection efficiencies for the polar angle θ of 30°, 60°, and 90° are plotted against the neutron fluence. Significant improvement is obvious for θ =30° but not for 60°.

Then in Fig. 19, the threshold charge for a layer half in the thickness, 267 μm, at θ =30° is compared with the detector of 535 μm at 90°. The threshold is about the same for zero fluence but the former is more than 80 % better at 5×10^{14} n/cm^2.

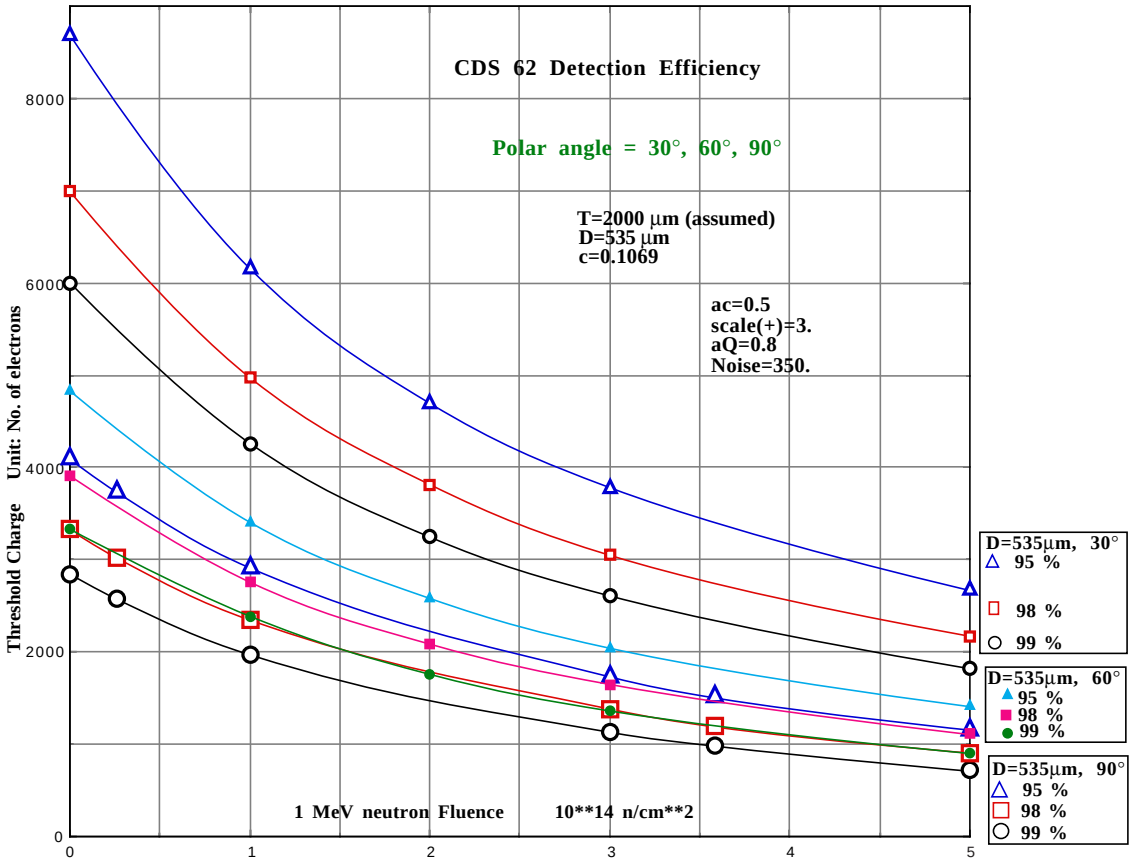

Fig. 18. Comparison of the threshold behavior for the polar angle of 30°,60°, and 90°.

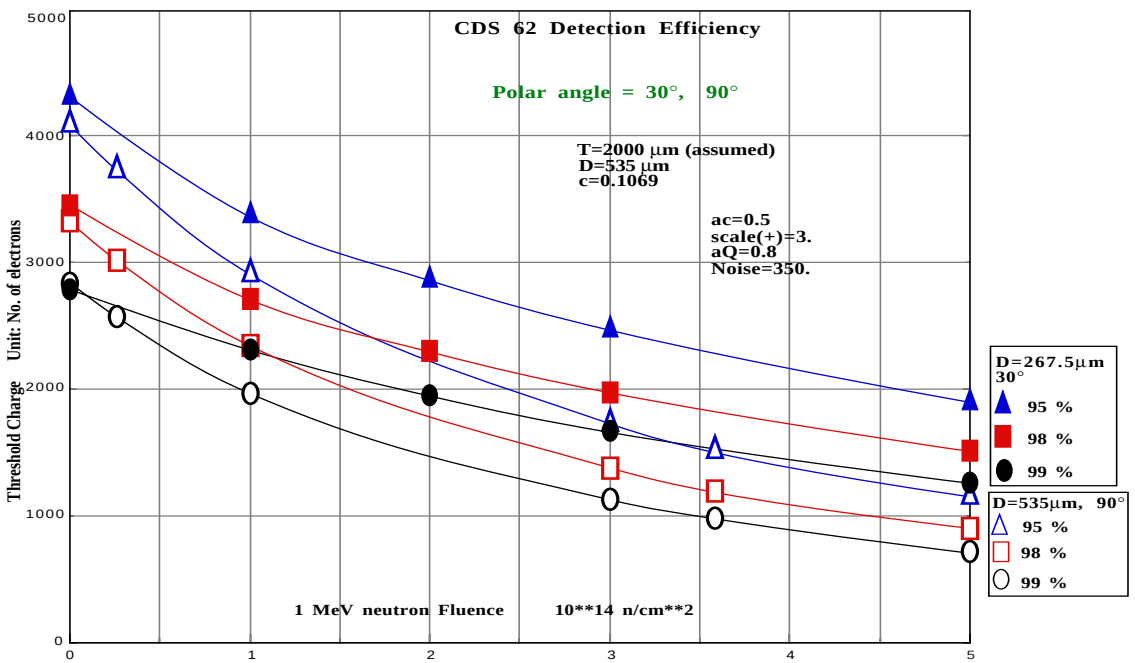

Fig. 19. 267.5 µm layer at θ=30° compared with 535 µm layer at 90°.

5. CONCLUSIONS

We have developed a simple model that describes the observed radiation damage by pion and neutron irradiation. The model assumes an exponential charge absorption factor as a result of radiation damage. It is locally multiplicative to the preexisted charge absorption term inherent to CVD diamond that linearly grow with the thickness of the material. The exponent of such factor must be a single constant corresponding to the charge trap distribution uniformly created by penetrating high energy particles and has to be proportional to the exposed fluence.

Integrating such local factor over the depth as the path length of the signal *e-h* pairs, one can calculate the induced charge for given sample thickness, coefficient c , and the fluence.

Such model reproduced quite well the general trend of the decrease of signals observed in pion and neutron irradiation experiment.

The factor to convert fluence into $\frac{1}{\lambda_{rad}}$ was found to be 0.0074 for π^+ (300 MeV/c) and 0.025~0.038 for neutron (~1 MeV) irradiation. Therefore neutrons are about a factor of 4 to 5 more damaging per particle. However the flux of the π^+ are about the same factor more copious and therefore the overall effect is not too different between two species in actual hadron collider environment.

The model reproduced the trend that the signals of high collection distance samples would decrease rapidly with increasing fluence whereas low collection distance samples would show greater endurance.

The decrease of the signal with increasing fluence is almost solely dependent on the initial size of the signal and not much dependent on the parameters such as the growth thickness, how it was lapped, or the growth parameter represented by the linear coefficient *c*. **Therefore once the signal is measured before irradiation, the signal after irradiation by π^+'s and neutrons can be well predicted.**

The model was further modified to include pulse height distribution with Landau fluctuation. In the calculation, the diamond was longitudinally divided into equal thickness slices, and on each slice, the energy deposit was fluctuated according to Landau distribution. The induced charge was calculated as the product of the energy deposit onto the slice and the distance traveled by the secondary electrons and holes from each slice and summed up. Gaussian type fluctuation was necessary to simulate the wide pulse height distribution observed. The fluctuation was applied to the linear term coefficient *c* and also to the final induced charge.

After adjusting the fluctuation parameters, we found a good agreement with the observed pulse height spectrum before the irradiation. Then switching the input parameter for the radiation induced charge absorption length, we obtained a spectrum for the irradiated sample that reproduced the observed spectrum quite well.

It was found that the change of the spectrum into narrower distribution, in relative scale, after the irradiation was not an intrinsic nature but due to the local inhomogeneity of the sample.

Due to the fact that the decrease of the average signal is almost solely dependent on the signal size of the unirradiated sample as stated above, it can also be said that **the model can predict the pule height distribution and hence the detection efficiency after irradiation by π^+'s or neutrons once the pulse height distribution is measured to determine the parameters on the non-uniformity of the sample**.

Therefore the radiation damage of diamond can be characterized in a universal formalism indepndent of the specifics of diamond samples.

The species of the irradiating particles is represented each by a single parameter.

The calculation was able to reproduce the observed average induced charge simply using the nominal 13 eV as the *e-h* pair creation energy which corresponds to 47 *e-h* pairs / μm. This fact indicates that the empirical value 17 eV corresponding to 36 *e-h* pairs / μm of diamond for a MIP is a mere reflection of the experimental cut imposed intentionally or implicitly due to finite dynamic range of the experimental setup and or the limited statistics.

The detection efficiency was calculated for several examples. Though high collection distance exhibits higher efficiency, the effect of the radiation is severer. A double layer configuration shows greater tolerance against radiation.

In the forward angles, the increase of the path length of the particles helps the average signal.

The good agreement of the calculated results with the observed data supports the basic assumption that there are equal contributions from electrons and holes, though not definitive.

ACKNOWLEDGMENT

We wish to thank Markus Friedl and Rudolf Wedenig for the communication supplying the detail information on the irradiation test.

Thanks also are due to Takuo Yoshida and Yukihiro Kato for pointing out available programs on Landau distribution and giving some help.

We have benefited from Jim Russ for discussions at various stages of this study.

We owe greatly to Hans Ziock who read the original manuscript carefully, checked the formulae, and made detailed corrections which made this document much clearer.

APPENDIX

Charge absorption factor : pre-existing linear term and radiation induced term.

The charge absorption through the travel from the point of charge creation ζ' to the point of the drifting ζ is a successive product of local exponential factors of the local charge absorption length λ_{CD} as a function of the depth, ζ, measured from the original substrate side as follows:

Absorption$(\zeta' \to \zeta)$

$$= \lim_{\Delta z \to 0} \exp\left\{-\frac{\Delta\zeta}{\lambda_{CVD}(\zeta')}\right\} \exp\left(-\frac{\Delta\zeta}{\lambda_{rad}}\right) \cdot \exp\left\{-\frac{\Delta\zeta}{\lambda_{CVD}(\zeta'+\Delta\zeta)}\right\} \exp\left(-\frac{\Delta\zeta}{\lambda_{rad}}\right) \cdot$$
$$\exp\left\{-\frac{\Delta\zeta}{\lambda_{CVD}(\zeta'+2\cdot\Delta\zeta)}\right\} \exp\left(-\frac{\Delta\zeta}{\lambda_{rad}}\right) \cdot \exp\left\{-\frac{\Delta\zeta}{\lambda_{CVD}(\zeta'+2\cdot\Delta\zeta)}\right\} \exp\left(-\frac{\Delta\zeta}{\lambda_{rad}}\right) \cdot \ldots\ldots \cdot$$
$$\exp\left\{-\frac{\Delta\zeta}{\lambda_{CVD}(\zeta-\Delta\zeta)}\right\} \exp\left(-\frac{\Delta\zeta}{\lambda_{rad}}\right) \exp\left\{-\frac{\Delta\zeta}{\lambda_{CVD}(\zeta)}\right\} \exp\left(-\frac{\Delta\zeta}{\lambda_{rad}}\right)$$

$$= \lim_{\Delta z \to 0} \exp\left[(-1)\left\{\frac{1}{\lambda_{CVD}\zeta'} + \frac{1}{\lambda_{CVD}(\zeta'+\Delta\zeta)} + \frac{1}{\lambda_{CVD}(\zeta'+2\cdot\Delta\zeta)} + \ldots + \frac{1}{\lambda_{CVD}(\zeta)}\right\}\Delta\zeta\right]$$
$$\exp\left(-\frac{\Delta\zeta + \Delta\zeta + \Delta\zeta + \ldots.. + \Delta\zeta}{\lambda_{rad}}\right)$$

$$= \exp\left[-\int_{\ell=\zeta'}^{\ell=\zeta} \frac{1}{\lambda_{CVD}(\zeta)}\, d\ell\right] \exp\left(-\frac{\zeta'-\zeta}{\lambda_{rad}}\right) .$$

Inserting

$\lambda_{CVD}(\zeta) = c\zeta$,

the above becomes

$$= \exp\left\{-\frac{1}{c}\left[\ell n(\ell)\right]_{\zeta'}^{\zeta}\right\} \exp\left(-\frac{\zeta'-\zeta}{\lambda_{rad}}\right)$$

$$= \exp\left\{-\frac{1}{c}\ell n\left(\frac{\zeta}{\zeta'}\right)\right\} \exp\left(-\frac{\zeta'-\zeta}{\lambda_{rad}}\right)$$

$$= \left(\frac{\zeta}{\zeta'}\right)^{\frac{1}{c}} \exp\left(-\frac{\zeta'-\zeta}{\lambda_{rad}}\right) .$$

Replacing ζ and ζ' with *T*-*z* and *T*-*z*', respectively, the above becomes

$$= \left(\frac{T-z}{T-z'}\right)^{\frac{1}{c}} \exp\left(-\frac{z-z'}{\lambda_{rad}}\right) .$$

Here *z* and *z*' are measured from growth side and *T* is the total as-grown thickness before any lapping on substrate side. Lapping is assumed to be only on substrate side.

REFERENCES

1) Thesis by S. Zhao: “Characterization of the Electrical Properties of Polycrystalline Diamond Films.” 1994.
2) M. Mishina : RD42 Note #13
3) D. Meier et. al., “Proton Irradiation Study of CVD Diamond Detector for High Luminosity Experiments at LHC”, Submitted to Proc. 2nd Int. Conf. On Radiation Effect on Semiconductor Materials , Detectors, and Devices, Florence, 98.
4) Vienna group: W. Adam, et al., RD42 Note 12.
5) Wedenig et. al. Presentation at RD42 Meetig at CERN, April 1998.
6) L Allers, et. Al., Neutron Damage of CVD Diamond, Paper contributed to DIAMOND 1996 Conference, Tours, France.
7) CMS Technical Proposal, CERN/LHCC 94-38, LHCC/P1, p114 (1994)
8) PDG
9) Neutron cross section
10) CERNLIB- CERN Program Library Short write-ups. G110. Also Geant User’s Guide PHYS332.